JGR Biogeosciences

RESEARCH ARTICLE

Key Points:

- Fluctuations in magnetization may occur due to microbially induced iron mineral transformation in hydrocarbon-contaminated aquifers
- Loss of magnetization is due to maghemitization (oxidation) and dissolution of magnetite grains
- Within the anoxic portions of the hydrocarbon plume, maghemitization occurs through anaerobic oxidation induced by microorganisms

Supporting Information:

Supporting Information may be found in the online version of this article.

Correspondence to:

E. A. Atekwana,
eaatekwana@ucdavis.edu

Author Contributions:

Formal analysis: Leonard O. Ohenhen, Joshua M. Feinberg, Alexis Stricker, Estella A. Atekwana
Funding acquisition: Lee D. Slater, Dimitrios Ntarlagiannis, Estella A. Atekwana
Methodology: Leonard O. Ohenhen, Joshua M. Feinberg, Estella A. Atekwana
Supervision: Joshua M. Feinberg, Estella A. Atekwana
Writing – original draft: Leonard O. Ohenhen, Joshua M. Feinberg, Estella A. Atekwana

Microbially Induced Anaerobic Oxidation of Magnetite to Maghemite in a Hydrocarbon-Contaminated Aquifer

Leonard O. Ohenhen[1,2] , Joshua M. Feinberg[3] , Lee D. Slater[4] ,
Dimitrios Ntarlagiannis[4] , Isabelle M. Cozzarelli[5] , Miriam Rios-Sanchez[6], Carl W. Isaacson[6],
Alexis Stricker[3], and Estella A. Atekwana[1,7]

[1]Department of Earth Sciences, University of Delaware, Newark, DE, USA, [2]Now at Department of Geosciences, Virginia Tech, Blacksburg, VA, USA, [3]Department of Earth & Environmental Sciences, Institute for Rock Magnetism, University of Minnesota, Minneapolis, MN, USA, [4]Department of Earth and Environmental Sciences, Rutgers University Newark, Newark, NJ, USA, [5]Geology, Energy & Minerals Science Center, U.S. Geological Survey, Reston, VA, USA, [6]Center for Sustainability Studies, Bemidji State University, Bemidji, MN, USA, [7]Now at Department of Earth and Planetary Sciences, University of California Davis, Davis, CA, USA

Abstract Iron mineral transformations occurring in hydrocarbon-contaminated sites are linked to the biodegradation of the hydrocarbons. At a hydrocarbon-contaminated site near Bemidji, Minnesota, USA, measurements of magnetic susceptibility (MS) are useful for monitoring the natural attenuation of hydrocarbons related to iron cycling. However, a transient MS, previously observed at the site, remains poorly understood and the iron mineral phases acting as reactants and products associated with this MS perturbation remain largely unknown. To address these unknowns, we acquired mineral magnetism measurements, including hysteresis loops, backfield curves, and isothermal remanent magnetizations on sediment core samples retrieved from the site and magnetite-filled mineral packets installed within the aquifer. Our data show that the core samples and magnetite packs display decreasing magnetization with time and that this loss in magnetization is accompanied by increasing bulk coercivity consistent with decreased average grain size and/or partial oxidation. Low-temperature magnetometry on all samples displayed behavior consistent with magnetite, but samples within the plume also show evidence of maghemitization. This interpretation is supported by the occurrence of shrinkage cracks on the surface of the grains imaged via scanning electron microscopy. Magnetite transformation to maghemite typically occurs under oxic conditions, here, we propose that maghemitization occurs within the anoxic portions of the plume via microbially mediated anaerobic oxidation. Mineral dissolution also occurs within the plume. Microorganisms capable of such anaerobic oxidation have been identified within other areas at the Bemidji site, but additional microbiological studies are needed to link specific anaerobic iron oxidizers with this loss of magnetization.

Plain Language Summary Iron is the fourth most abundant element in the Earth and can be cycled by microorganisms from one form to another often accompanied by the precipitation of different iron mineral phases. Some of these minerals have magnetic properties resulting in the magnetization of their host rocks. Some studies have documented that the magnetic minerals can be cycled by microorganisms resulting in the increase or loss of the magnetization. The mechanism by which this happens is not well understood. In this study, we conducted an experiment at a hydrocarbon-contaminated site where iron cycling is occurring to better understand the cause of this loss of magnetization and the accompanying mineral changes associated with this process. Our results show the loss of magnetization is caused by the oxidation of magnetite (a highly magnetic mineral) to maghemite (a less magnetic mineral). This oxidation occurs under oxygen-limiting conditions caused by microorganisms. However, the oxidation process does not account for all the loss in magnetization, leaving us to suggest dissolution may also be contributing to the loss of magnetization. Our results support that microorganisms may have the potential to mediate changes in the magnetic properties of Earth materials.

1. Introduction

The cycling of iron (Fe) is an essential process that occurs in most environments on Earth (Markovski et al., 2017) and is essential to the fate, transport, and cycling of nutrients and contaminants in the environment (Hansel et al., 2005). This participation of Fe in biological cycles is related to its ability to exist in a multitude of dissolved and solid phases, all of which respond to dynamic changes in biotic and abiotic conditions that may alter and/or

precipitate new Fe phases (Aristovskaya, 1974; Kappler & Bryce, 2017; Li et al., 2009). In natural environments, the abiotic transformation of Fe is driven by parameters such as pH, temperature, oxygen (O_2), and the presence of electron donors, as well as particular types of organic compounds that may promote the oxidation, reduction, or dissolution of Fe-bearing minerals and compounds (Ionescu et al., 2015). Biotic (microbial) transformation of Fe is carried out by a diverse group of microorganisms through the process of oxidation or reduction. The microbial oxidation of Fe occurs through photosynthetic Fe (II) oxidation or the use of O_2 or nitrate (NO_3) as a terminal electron acceptor (Ionescu et al., 2015; Liu et al., 2018). During the microbial reduction of Fe, a common pathway is the reduction of Fe (III) minerals such as ferrihydrite by dissimilatory iron-reducing bacteria leading to the formation of different Fe mineral phases (e.g., goethite, lepidocrocite, green rust, ferran calcite, siderite, pyrite, and magnetite; Hansel et al., 2005; Kappler et al., 2021; Markovski et al., 2017). These biogeochemical transformations of Fe minerals are a major feature in environments such as freshwater-saltwater interfaces (McAllister et al., 2015) and hydrocarbon-contaminated environments (Atekwana et al., 2014; Lund et al., 2017; Rijal et al., 2010, 2012; Tuccillo et al., 1999).

In hydrocarbon-contaminated environments, the presence of contaminants can alter the physiochemical and biological properties of the subsurface (Abbas et al., 2018). These perturbations can cause chemical and microbial imbalances, which may trigger abiotic and/or microbially induced transformations of Fe minerals (Truskewycz et al., 2019). The highly bio-reactive zones found at hydrocarbon-contaminated sites are ideal environments for the investigation of field-scale Fe transformations (Atekwana & Atekwana, 2010; Atekwana et al., 2014). Several studies have documented Fe mineral (trans)formation in hydrocarbon-contaminated soils (Atekwana et al., 2014; Baedecker et al., 1992; Lovley, 1990; Rijal et al., 2010, 2012). A common theme in these studies is the microbial transformation of Fe minerals, where dissimilatory iron-reducing bacteria utilize carbon sources in hydrocarbons to reduce Fe(III) to Fe(II; Anderson & Lovley, 2000) leading to the precipitation or transformation of different Fe mineral phases (Atekwana et al., 2014; Baedecker et al., 1992; Lovley, 1990; Rijal et al., 2010, 2012). These mineral transformations have a profound effect on the arsenic concentration in groundwater (Cozzarelli et al., 2016; Rawson et al., 2016) and the magnetic properties of natural sediments (Maxbauer et al., 2016a), and thus magnetic methods can be used to investigate and quantify Fe cycling.

Magnetic susceptibility (MS) is one of the most commonly used magnetic tools for monitoring microbially mediated Fe cycling (Atekwana et al., 2014; Mewafy et al., 2011; Porsch et al., 2010; Rijal et al., 2010, 2012). Porsch et al. (2010) noted magnetite formation by microorganisms during ferrihydrite reduction in laboratory experiments and concluded that MS can serve as a suitable tool for investigating Fe transformations, due to variations in MS response by different Fe minerals. Similar studies at sites contaminated by hydrocarbons, explored the use of MS to investigate iron mineral transformations and established a link between increase in MS and magnetite concentrations. Rijal et al. (2010) reported elevated MS values coincident with microbial activity at the top of the water table fluctuation zone (WTFZ) in hydrocarbon-contaminated sediments at a former military site in Czech Republic. Additionally, studies by Mewafy et al. (2011) and Atekwana et al. (2014) at the hydrocarbon-contaminated site investigated for this work, documented elevated MS values across the WTFZ associated with the precipitation of magnetite and biodegradation of hydrocarbon by microbes. These studies highlight the potential for the use of MS as a tool for investigating microbially mediated Fe mineral transformations in the subsurface.

The continuous measurements at hydrocarbon-contaminated sites have shown that MS signals are transient (Ameen et al., 2014; Lund et al., 2017), complicating the interpretation of Fe mineral cycling. Ameen et al. (2014) documented decreased MS values associated with hydrocarbon degradation and proposed dissolution of magnetite as the cause for this loss in MS. This transient nature of elevated MS values has also been documented by Lund et al. (2017) at the Bemidji site, where MS measurements showed ~90% loss between 2011 and 2015 (Figure S4 in Supporting Information S1). The ability to capture both the waxing and waning of MS signals related to hydrocarbon degradation demonstrates the utility of MS as a tool for investigating the biogeochemical cycling of Fe (Atekwana et al., 2014; Byrne et al., 2015). Nonetheless, there are ambiguities inherent to MS measurements that may limit their use, such as nonuniqueness in characterizing the specific magnetic mineralogy, concentration, and grain size distribution that occurs within a sample (Liu et al., 2012). Thus, our ability to use MS as a tool to investigate the biogeochemical cycling of Fe requires a more detailed understanding of magnetic mineralogy, mineral transformation products, and properties.

In this study, we investigate the iron mineral transformations associated with the loss of MS recorded at a hydrocarbon-contaminated site near Bemidji, Minnesota (Figure S4 in Supporting Information S1). Using magnetic

methods that are more advanced and diagnostic than MS data alone, we build on previous magnetic measurements at the Bemidji hydrocarbon-contaminated site (Atekwana et al., 2014; Lund et al., 2017). Mineral packets constructed of known mineralogy were emplaced within the water table fluctuation zone at different locations at the site and subsamples were periodically retrieved for a longitudinal study. Samples were characterized using low-temperature magnetometry and a variety of hysteresis and remanence measurements. Similar measurements were performed on retrieved core samples to determine the transformation products and the underlying transformation mechanisms at the site. This unique in situ experiment allowed us to control the conditions by using known reactants and making intermittent measurements to monitor changes in the magnetic signals and mineralogy which is typically only possible in laboratory settings. This approach is useful here for understanding the correlation between microbial communities and iron mineral phases in nature (Byrne et al., 2015, 2016; Hansel et al., 2003, 2005). Our results show that magnetization decreased in the mineral packets with time owing to a spatially variable combination of maghemitization and mineral dissolution at the site. Furthermore, the magnetic measurements indicate elevated maghemite production at the center of the plume, known to be a strongly anoxic environment, suggesting that microorganisms within the WTFZ of the plume are facilitating anaerobic oxidation of magnetite to maghemite.
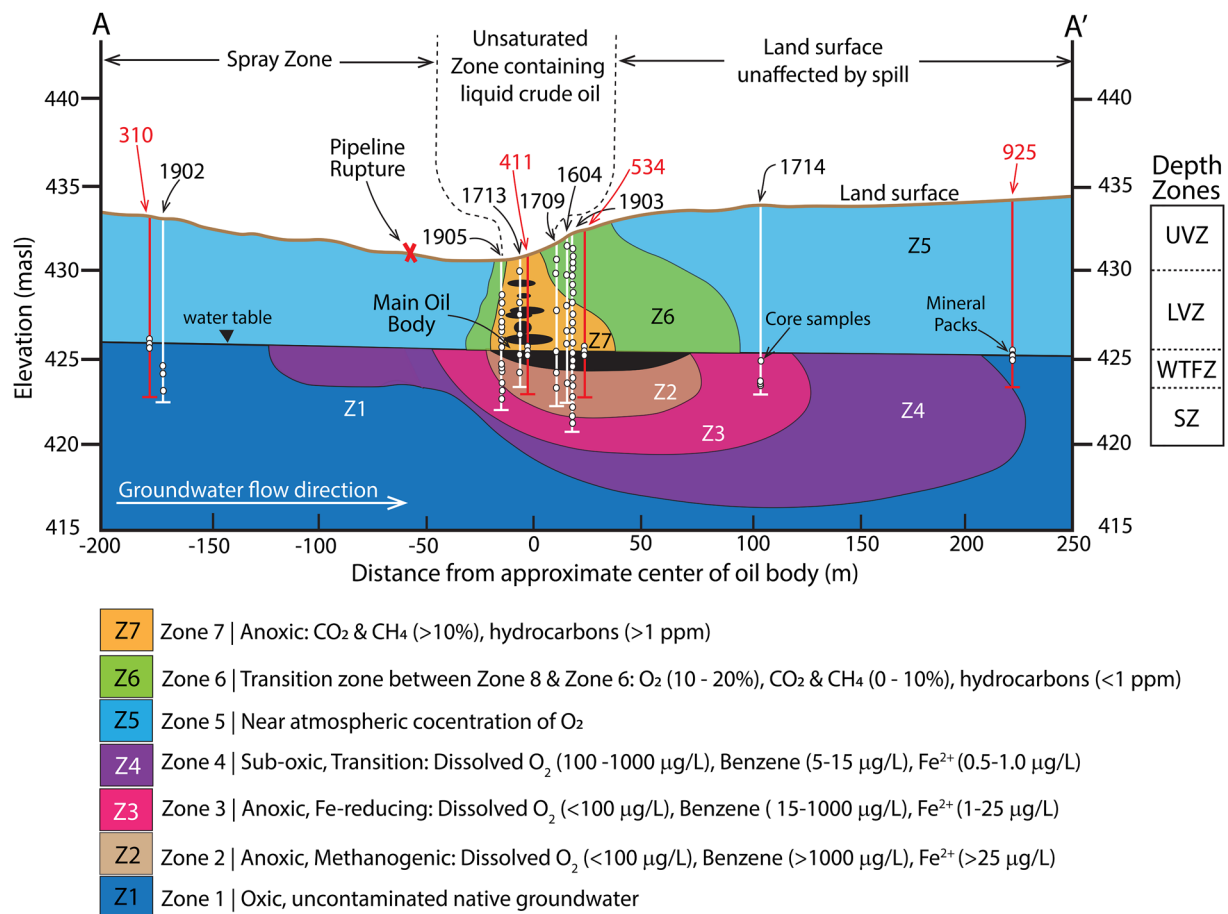
1.1. Study Site

The study site is the National Crude Oil Spill Fate and Natural Attenuation Research Site near Bemidji, Minnesota, United States which is managed by the U. S. Geological Survey (USGS) for long-term research on hydrocarbon degradation. In August 1979, a pipeline rupture occurred at this site spilling about 1.7 million liters of oil (Delin et al., 1998). The oil sprayed over an area of 6,500 m^2 southwest of the pipeline (spray zone, Figure 1) and subsequently pooled in low topographic areas and a nearby wetland, covering around 2,000 m^2 (Essaid et al., 2011). The oil infiltrated into the subsurface through the unsaturated zone to the water table resulting in three oil bodies named the North, Middle and South oil bodies (Figure 1). The cleanup effort at the site involved pumping from surface pools (about 1.1 million liters), burning, and excavation (about 200,000 L). At the end of the cleanup effort in 1980 about 400,000 L of oil remained in the ground due to oil seepage (Cozzarelli et al., 2016; Essaid et al., 2011; Lund et al., 2017). The site geology consists of a roughly 20-m thick layer of moderately calcareous silty sand and outwash glacial deposits overlying clayey till of unknown thickness (Bennett et al., 1993). Water table depth at the site ranges from 0 m at an unnamed lake east of the North oil body to a maximum of about 11 m below land surface (Delin et al., 1998; Essaid et al., 2011; USGS, 2021). Water table fluctuations of about 1 m annually across the site cause free-phase hydrocarbons to move up and down with the water table, causing adsorption of the hydrocarbons onto the aquifer solids, forming the smear zone with variable thickness (Atekwana et al., 2014). In the North oil body, the thickness of the smear zone was measured to be more than 2 m and the maximum oil saturation is 0.74 in the down-gradient from the oil body (Essaid et al., 2011). The dissolved-phase plume, which contains dissolved BTEX (benzene, toluene, ethylbenzene, and xylene) occurs in the saturated zone and migrates downgradient along the direction of groundwater flow (Figure 1). This study is located within the uncontaminated zone, free-phase hydrocarbons, and dissolved phase plume of the North oil body, which has been the focus of intensive geochemical and microbial studies (Amos et al., 2012; Beaver et al., 2016, 2021; Bekins et al., 2016; Cozzarelli et al., 2010; Fahrenfeld et al., 2014).

In the North oil body, eight geochemical zones have been classified, five within the saturated zone and three within the unsaturated zone, which are broadly classified into the anoxic, transition, and oxic zones (Baedecker et al., 1993; Delin et al., 1998). Figure 2 is a generalized description of the geochemical zones within the North oil body. Although the schematic is based on historical data, the main geochemical attributes remain fairly consistent over time. Baedecker et al. (1993) and Bennett et al. (1993) provide additional details of the geochemistry of these zones. The geochemical and microbiological studies suggest that methanogenesis is the dominant reaction at the center of the plume, where a methanogenic community is present (Beaver et al., 2021). The microbial communities in the study site are characterized by distinct vertical redox zonation. These distinct redox zonations and their corresponding microbial communities are discussed in detail in a recent study by Beaver et al. (2021). These vertical zonations are depth zones defined by elevation measured in meters above sea level (masl), which include the upper vadose zone (UVZ; elevation >429 masl), lower vadose zone (LVZ; elevation between 425.5 to 429 masl), smear zone or water table fluctuation zone (WTFZ; elevation between 423.5 to 425.5 masl), and saturated zone (SZ; elevation <423.5 masl). Here, we combine the smear zone and the free-product zone of Beaver
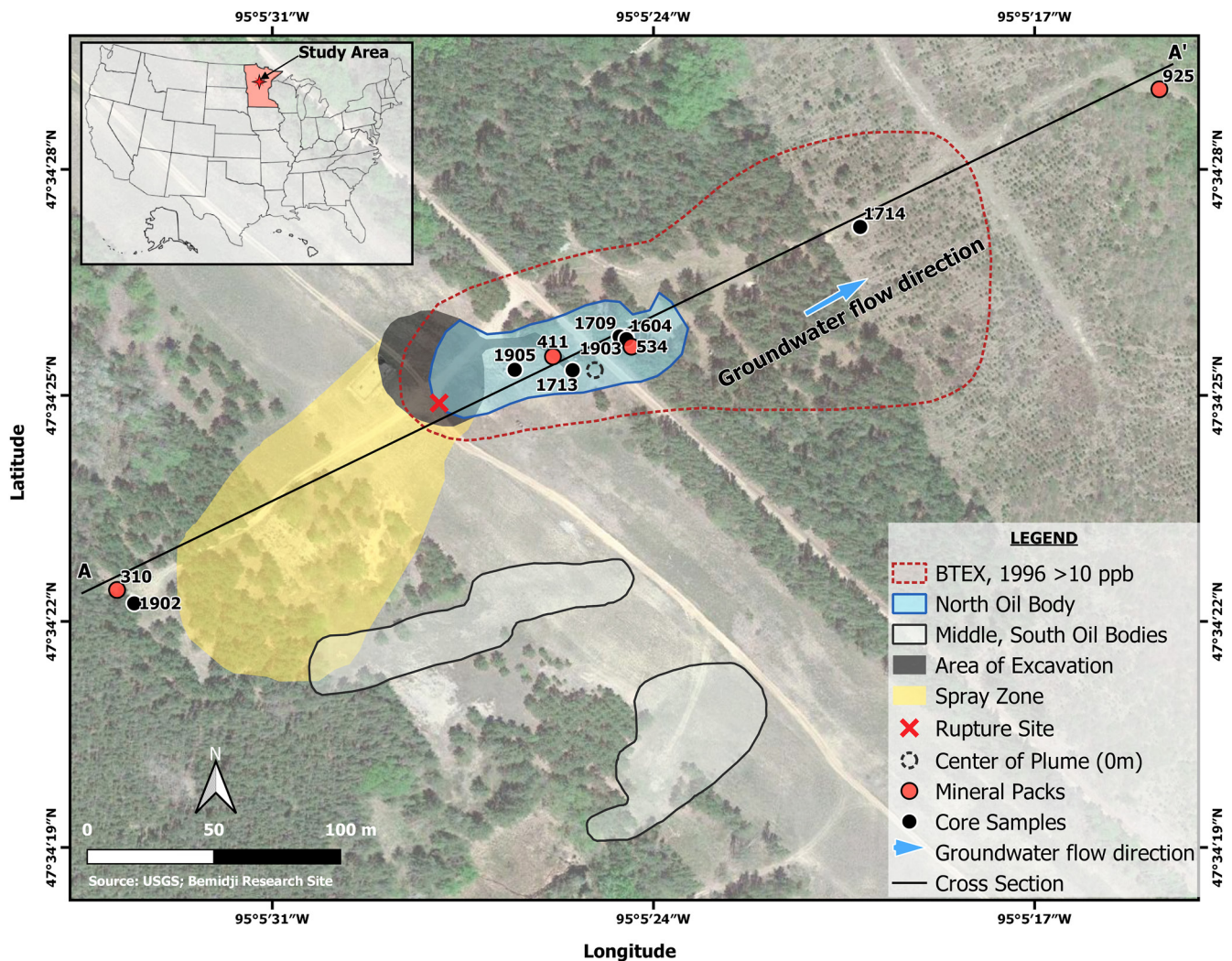
Figure 1. Study site showing locations of magnetite packs and core samples (modified from USGS, 2020). Transect A–A' is shown in Figure 2. Mineral columns are shown as red circles. Core samples are shown as black circles for core samples retrieved in 2016 (1604), 2017 (1713, 1709, 1714), and 2019 (1902, 1903, 1905).

et al. (2021) to the WTFZ. *Smithella* was the dominant genus found in the free-phase oil zone followed by the hydrogenotrophic methanogen, *Methanoregula*. Other microorganisms included *Candidatus* Yanofsky bacteria, *Desulfospotosinus* and *Pelolinea*. These bacteria, particularly *Smithella* and *Methanoregula*, play a role in the biodegradation of the free-phase oil within this zone. Within the smear zone, the uncultured *Coriobacteriaceae* is the most dominant in the smear zone. Other microbial communities within the smear zone include *Thermincola*, *Paenibacillus*, and *Beijerinckia* (Beaver et al., 2021). The lower part of the smear zone is methanic and concomitant with observations of magnetic mineral enrichment and an increase in MS (Atekwana et al., 2014; Beaver et al., 2021; Lund et al., 2017). The lower vadose zone is the most microbially diverse zone, dominated by methanotrophic populations (*Polaromonas*), iron reducers (*Geobacter*), and iron oxidizers (*Rhodopseudomonas*; Beaver et al., 2021). However, *Geobacter* which has been linked to iron reduction at the site is of relatively low abundance highlighting that geochemical functions and mineral transformations can be performed by low-abundance microbes (Fahrenfeld et al., 2014). Other microorganisms isolated within the lower vadose zone include *Comamonadaceae*, *Methylocystis* (a common methane-oxidizer), and *Devosia* (Beaver et al., 2021). The upper vadose zone is an aerobic zone, inhabited by mainly *Actinobacteria* and *Acidobacteria* phyla, which are common soil bacteria (Beaver et al., 2021).

Figure 2. Characterized geochemical zones across the north oil body of the study site (modified from Delin et al., 1998; Cozzarelli et al., 2016). Magnetite pack columns are shown in red vertical lines. Core samples are shown in white vertical lines for core samples retrieved in 2016 (1604), 2017 (1713, 1709, 1714), and 2019 (1902, 1905, 1903). The upper vadose zone (UVZ) represents elevation >429 masl, lower vadose zone (LVZ) represents elevation between 425.5 and 429 masl, water table fluctuation zone (WTFZ) represents elevation between 423.5, and 425.5 masl and saturated zone (SZ) represents elevation <423.5 masl.

2. Methodology

2.1. Sampling

Two sets of samples were obtained from the site (Tables S1 and S2 in Supporting Information S1): (a) Core samples of aquifer sediment retrieved from the site (black circles, Figure 1 and white lines, Figure 2) and (b) samples of potentially reactive mineral standards (mineral columns) that had been placed within the WTFZ of monitoring wells in different locations at the Bemidji site (red circles, Figure 1 and red lines, Figure 2).

Core samples were retrieved from 7 continuous cores acquired from different sites within and outside the plume for 2016, 2017, and 2019 (Figures 1 and 2). Five cores were retrieved from the free-phase hydrocarbons of the North oil body; one in 2016 (1604), two in 2017 (1709 and 1713), and two in 2019 (1903, 1905). Additionally, one core was retrieved within the dissolved phase of the plume (2017 [1714]) and another core was retrieved upgradient from the plume (2019 [1902]). Cores were retrieved through percussion drilling using a core barrel containing either a one- or 2-inch polycarbonate liner that was pushed through the sediment using a stem auger. For core sections within the saturated zone, a sample-freezing shoe drive was used to retain water from the aquifer (Murphy & Herkelrath, 1996). Samples were collected at different depths for each core, but sampling density was higher during the 2019 field campaigns as compared to the 2016 and 2017 field campaigns (Figure 2).

The mineral columns, consisting of alternating sand, ferrihydrite packets, and magnetite packets in a vertical sequence (Figure S5 in Supporting Information S1) were deployed in monitoring wells across the water table fluctuation zone (WTFZ), with approximately half the mineral column below the water table (Figure S5b in

Supporting Information S1) at different locations within and outside the North oil body, respectively. Two of the mineral columns were located within the free phase of the plume (411 and 534) and two outside of the plume; one was located up gradient (310) and the other was down gradient (925) from the oil pool according to the general groundwater-flow direction (Figures 1 and 2). Column 411 was deployed within the "pit" (2 m from the center of the oil pool), which refers to a topographic depression located near the center of the oil pool, an area of enhanced recharge (Baedecker et al., 2018; Delin & Herkelrath, 2017) and possibly enhanced microbial activity (Bekins et al., 2005). Column 534 is located ~25 m from the center of the oil pool. For this study, we present primarily the measurements made on the magnetite packs since the goal of this project is to investigate the loss of MS associated with transformation of magnetite at the site. The measurements made on the ferrihydrite packs are used here only cursorily. The magnetite packs consisted of packets of magnetite and quartz sand (5% magnetite with an average grain size of 800.5 μm mixed with 95% quartz of average grain size 286.2 μm). Columns 411, 534, and 310 contained three magnetite packs, whereas column 925 contained just two magnetite packs (Figure S5b in Supporting Information S1). Three (534, 411, and 925) columns were installed in November 2018 and retrieved from the boreholes in June and October 2019, while column 310 was installed in June 2019 and retrieved in October 2019. The mineral packets were sampled by puncturing the nylon sleeve with a wooden spatula and approximately 1 g of material was removed from each mineral layer. Samples were placed in a glass vial, purged with argon, and crimp sealed.

All core samples and mineral packs retrieved from the site were stored at 4°C on ice and transported to the Institute for Rock Magnetism at the University of Minnesota for magnetic measurements. Samples were maintained in a freezer prior to magnetic measurements. Portions of the original mineral packet samples not deployed at the site were also retained and served as controls for measurements.

2.2. Magnetic Analyses

To determine the magnetization, relative particle size distribution, and magnetic mineralogy of the samples, we performed magnetic analyses such as hysteresis loops, backfield curves and low temperature magnetic properties on the dried core samples and magnetite packets. Hysteresis loops and backfield curves were measured using a vibrating sample magnetometer (Princeton MicroMag) at room temperature and applied external magnetic fields of ± 1 T. Since the samples were collected as loose sediment, samples were interred within nonmagnetic glue and allowed to dry in a fume hood before measurements were collected. The hysteresis loop is a cycle of magnetization that illustrates the complex relationship between magnetization and external magnetizing field (Text S1 in Supporting Information S1; Telford et al., 1990). The properties obtained from the hysteresis loops, such as saturation magnetization (M_s), saturation remanence (M_r), and bulk coercivity (B_c) are useful for determining the properties of the magnetic sample (Cornell & Schwertmann, 2003). The information measured directly, or inferred from the hysteresis parameters, is related to the sensitivity of each measurement or parameter. For example, M_s is sensitive to the magnetic concentration and thus provides information about the concentration of iron in the sample. M_r is sensitive to the grain size and magnetic concentration, and B_c is sensitive to the grain size, where the larger the B_c, the smaller the grain size and vice versa. The hysteresis loops were analyzed using the methods of Jackson and Solheid (2010) and plotted to determine magnetic saturation, grain size and distribution domain state of the samples. The backfield curves were measured under zero field to obtain the coercivity of remanence (B_{cr}). B_{cr} is a measure of the field needed to drive the M_r to zero. Most environments contain a complex mixture of magnetic minerals with different environmental histories; a robust interpretation involves "unmixing" the behavior of a sample to characterize the magnetic mineral assemblages (Heslop & Dillon, 2007). Coercivity spectra from backfield remanence curves were evaluated using the MaxUnmix software (Maxbauer et al., 2016b). Additional details about the hysteresis measurements and backfield curves are provided in Texts S1 and S2 of Supporting Information S1.

A Quantum Design Magnetic Properties Measurement System (MPMS) instrument was used to measure the low-temperature magnetic properties of the samples. The usefulness of low-temperature magnetic measurements is the characteristic behavior of different iron minerals, which is useful to distinguish between different mineral phases (Housen et al., 1996). Certain iron minerals exhibit low-temperature transitions, which are useful for both the identification of primary and secondary iron minerals in a sample (Özdemir & Dunlop, 2010). Sediment samples were packed firmly between layers of quartz wool to prevent grain rotation and sealed inside a pharmaceutical gelatin or bicarbonate capsule. Two types of measurements were collected: (a) field cooled (FC)

remanence, which involves heating from 10 to 300 K (room temperature) at 5 K steps after cooling from room temperature in a 2.5 T field, and zero-field cooled (ZFC) remanence, which involves cooling in a zero field but applying a pulsed saturation isothermal remanent magnetization (SIRM) of 2.5 T at 10 K; and (b) cooling and warming curves of room-temperature pulsed saturation isothermal remanence magnetization at 2.5 T (RTSIRM).

An AGICO MFK1-FA Susceptibility Bridge with CS4 Furnace was used to collect high-temperature magnetic susceptibility measurements using a field of 300 A/m with a frequency of 976 Hz cycled from 20 to 680°C and back to 50°C.

Hysteresis loops and backfield measurements were collected for all core samples and magnetite packet samples (78 samples). However, for some core samples, the coercivity spectra could not be unmixed due to poor signal-to-noise ratio. Hysteresis loop measurements on the ferrihydrite packs are found in Table S2 of Supporting Information S1. Due to time constraints involved in low-temperature magnetometry experiments, the FC-ZFC and RTSIRM measurements were restricted to the central magnetite packet of each column retrieved in June and October 2019 and nine core samples from 2016, 2017, and 2019 from within and outside the plume retrieved from various depths and zones (Table S1 in Supporting Information S1). Temperature-dependent magnetic suscepti-bility measurements were restricted to six representative samples from 2016 to 2017 core samples (Figure S13 in Supporting Information S1). For the magnetite packets, a sample of the original unaltered magnetite used in the preparation of magnetite packs was used to assess deviations from the starting magnetite and serve as the control sample. Thus, magnetic measurements performed on this control magnetite packet are denoted as fresh magnetite (FM) in this work.

2.3. Statistical Analyses

To examine the existence of spatial variability across the site with respect to the center of the oil pool, we performed an analysis of variance (ANOVA) for the magnetite packets retrieved in October 2019 for the 411, 534, and 925 magnetite packets with an 11-month interment. The purpose was to analyze if there are statistical differences between the magnetite samples retrieved at different locations within the aquifer and the FM. We measured 30 hysteresis loops for the FM, the central, and bottom magnetite packets of columns 411, 534, and 925 only. The measurements were restricted to the central and bottom magnetite packs to normalize the meas-urements with column 925, which contains only two magnetite packets. Thirty repeated hysteresis loops for each magnetite packet were made by alternating the vibrating frequency of each measurement between 0.2 and 1.0. This variation in the vibrating frequency allows for subtle variability in each measurement of the subsamples used in the ANOVA.

To examine the existence of a depth variability in the magnetization within the aquifer, we performed ANOVA for the core samples retrieved in 2019 (1903 and 1905 samples) since the 2019 sampling had the greatest sampling density for all core samples retrieved. The purpose of this was to examine if there are statistical differences between core samples retrieved from different depths within the oil pool. The core samples from the different depths were classified into depth zones according to elevation in masl. In total, thirty-three (33) core samples (UVZ - 6, LVZ - 12, WTFZ - 9, LVZ - 6) were used for the ANOVA.

The response variable used for the ANOVA test was M_s, which is sensitive to the concentration of magnetic minerals in each sample. This is useful here to test the variability in the magnetic concentration across the aquifer and with depth. The null hypothesis for the ANOVA performed on the magnetite packets was that there is no difference between the samples retrieved across the aquifer and the fresh magnetite samples. The null hypothesis for the ANOVA performed on the core samples was that the M_s for samples in the UVZ, LVZ, WTFZ, and SZ are equal. An alpha value of 0.05 was specified for both ANOVA tests. The statistical analyses were performed using JMP Pro 15 software.

2.4. Microscopy

Surface textures, crystal size, and elemental composition of samples were determined using scanning electron microscopy (SEM) and energy dispersive X-ray spectroscopy (EDS). The samples were prepared for imaging by sonicating the samples in an alcohol bath for 6 minutes and separating the magnetic fraction of the samples using a bar magnet when the grain size was sufficiently large enough to allow for separation with a magnet. Where
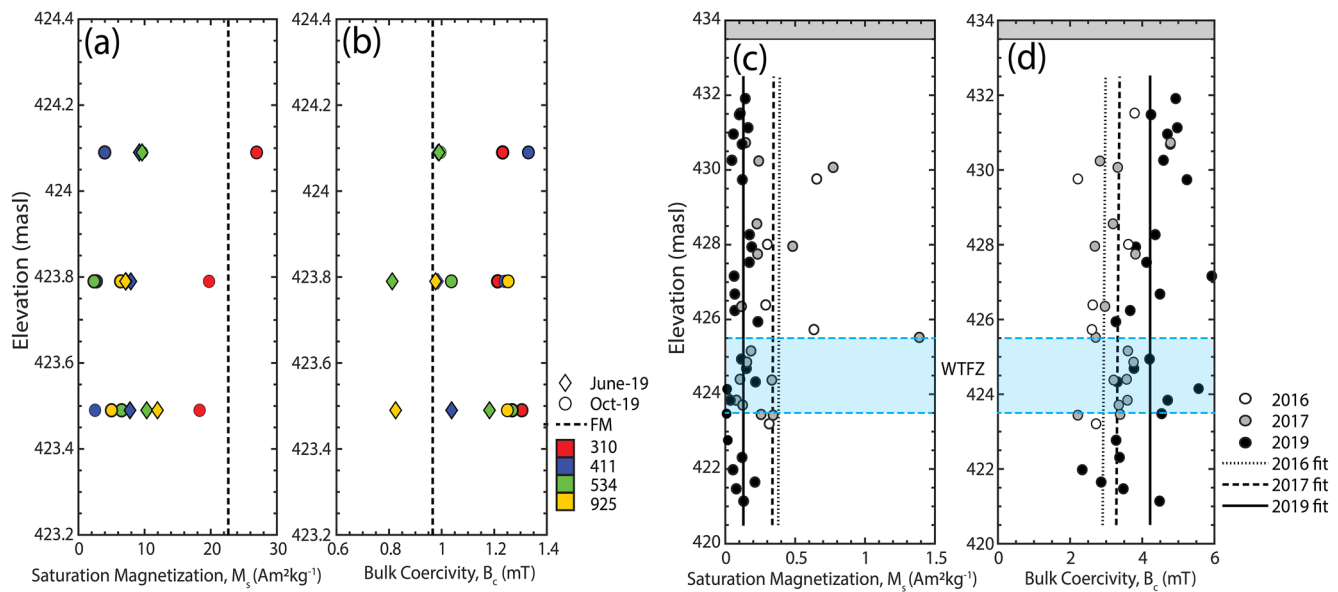
Figure 3. Decrease in magnetization and corresponding increase in bulk coercivity (B_c) in time for magnetite packs and core samples. Plot of (a) saturation magnetization (M_s) and (b) bulk coercivity (B_c) with depth for magnetite packs. Depth values for the magnetite packs are not actual depths but were normalized to average depth for each pack for visual representation. Dashed lines represent M_s and B_c of the fresh magnetite, respectively. Diamond symbols are samples retrieved in June 2019; circle symbols are samples retrieved in October 2019. Red symbols represent column 310 magnetite packs, blue symbols represent 411 magnetite packs, green symbols represent 534 magnetite packs, and yellow symbols represent 925 magnetite packs. Plot of (c) saturation magnetization (M_s) and (d) bulk coercivity (B_c) for core samples retrieved in 2016 (1604 core sample), 2017 (1713, 1709, and 1714 core samples), and 2019 (1903 and 1905 core samples). The shaded blue regions shows the water table fluctuation zone. White circles represent core samples retrieved in 2016, gray circles represent core samples retrieved in 2017, and black circles represens samples retrieved in 2019. The vertical lines for 2016, 2017, and 2019 are the average values for each year.

grains could not be successfully separated with a magnet, a small sample consisting of both magnetic and quartz grains was used for SEM imaging. Three different samples were prepared for the microscopic analysis, FM, column 534 magnetite pack (October 2019), and 2019 (1905-9-8) core sample. SEM imaging and EDS analysis were performed using a JEOL JSM-6500F Field Emission Scanning Electron Microscope.

3. Results

3.1. Magnetic Measurements

3.1.1. Hysteresis Properties

Derived parameters from the hysteresis data for core samples and magnetite packs are summarized in Table S1 of Supporting Information S1 (results of the hysteresis properties of the ferrihydrite packs are discussed in Text S3 of Supporting Information S1). For each core sample or magnetite pack, we made hysteresis measurements on either single or multiple (three) subsamples depending on the available sample size. For the magnetite packs, there is a precipitous decrease in M_s with time for samples within the plume from about 22.68 Am^2 kg^{-1} (FM) to a minimum of about 2.51 Am^2 kg^{-1} (411) and 2.36 Am^2 kg^{-1} (534) representing ~90% drop in M_s during the <1-year interval that the magnetite packs were interred within the smear zone (Figure 3a). Magnetite packs outside the plume also show a similar decrease in M_s with time, though the extent of the decrease varies in relation to position of the plume. Magnetite packs from 310, upgradient from the plume, showed the least decrease in M_s (18.32 Am^2 kg^{-1}) or about 19% during its four-month interment (Figure 3a). Note that the first magnetite pack in the 310 column showed an M_s value of 26.94 A.m.^{2} kg^{-1}, which is higher than the FM; perhaps the magnetite in the sample was concentrated beyond 5%, since 310 column was installed at a different time from the other mineral columns. The minimum M_s for magnetite packs from 925 was 5.00 Am^2 kg^{-1} and represents a 78% decrease in M_s with time, which was unexpected given that this site is noted outside the boundary of the dissolved phase plume (Figure 1). However, a revised plume map from the Bemidji site reveals that the dissolved phase plume extends beyond the location of 925 column (Bekins et al., 2016) and minor enhancement of MS within the WTFZ was also previously recorded in wells around this vicinity (Atekwana et al., 2014). Thus, for this study,
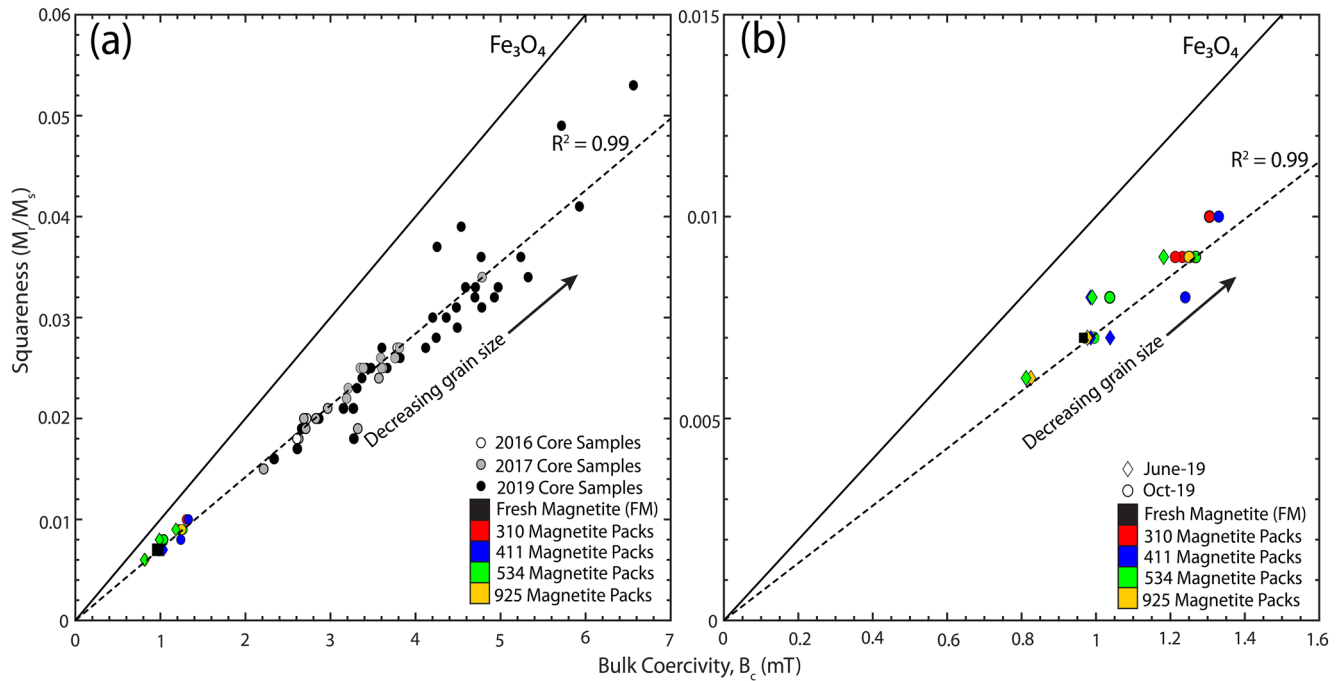
Figure 4. Squareness (M_r/M_s) versus B_c for (a) magnetite packs and core samples, (b) magnetite packs only. Symbols as in Figure 3. The line for pure stoichiometric magnetite (Fe_3O_4) is empirically derived from Wang and Van der Voo (2004).

the 925 magnetite packs are considered within the dissolved phase plume of the North oil body. Along with the decrease in M_s, there is a subtle, but persistent increase in the B_c, from about 0.97 mT (FM) to a maximum B_c of 1.33 mT (411), 1.27 mT (534), 1.25 mT (925), and 1.30 mT (310; Figure 3b). For the core samples, M_s ranged between 1.39 and 0.01 Am^2 kg^{-1} with an average of 0.21 Am^2 kg^{-1} and B_c ranged between 2.21 and 5.93 mT. A plot of M_s and B_c versus depth for 2016, 2017, and 2019 core samples occurring within the free phase of the plume, shows a decrease in average M_s with time and like the magnetite packs an inverse relationship for the yearly average B_c (Figures 3c and 3d).

Core samples and magnetite packs show a linear relationship between squareness (M_r/M_s) and B_c and the magnetite packs are closer to the slope of magnetite samples of Wang and Van der Voo (2004) (Figure 4a). The deviation of the magnetite samples to plot along the magnetite line of Wang and Van der Voo (2004) could be due to the presence of diamagnetic quartz grains in the magnetite packs. Close examination of the magnetite packs shows that the October 2019 samples have higher coercivities and M_r/M_s ratios than the fresh magnetite (FM; Figure 4b). These changes in magnetic properties occur both for samples within and outside the plume. The Day plot, which is often used to differentiate the bulk average magnetic domain state, shows that all samples fall within the multidomain (MD) region (Figure 5, Day et al., 1976). However, different trend lines can be fitted for the core samples and magnetite packs, which could be indicative of different grain size distributions, cation substitution, partial oxidation, and/or provenance (Dunlop & Özdemir, 1997). The core samples also appear to show a temporal trend toward the finer-grained single domain (PSD) region, with the 2019 core samples showing higher M_r/M_s and lower B_{cr}/B_c values.

Unmixing of the backfield remanence measurements is a technique that fits multiple log-normal distributions to the derivative of the backfield remanence measurements (Figure S7 in Supporting Information S1). In Figure 6a, the dispersion parameter (DP) describes the breadth of each log-normal distribution in a sample (Figure S2 in Supporting Information S1), where the higher the DP, the broader the coercivity distribution and vice versa. The median coercivity (Bh) of the log-normal distribution can be used to differentiate between fine versus coarse grain sizes. Each core sample shows two populations of magnetic grains during coercivity unmixing (Figures S7d–S7l in Supporting Information S1), and these populations appear as two distinct clusters (Figure 6a). One of the clusters centers at Bh = 10 mT and DP = 4 mT, which is broadly similar to the detrital magnetite component ("detrital and extracellular magnetite (D + EX)") described by Egli (2004), though we recognize that they
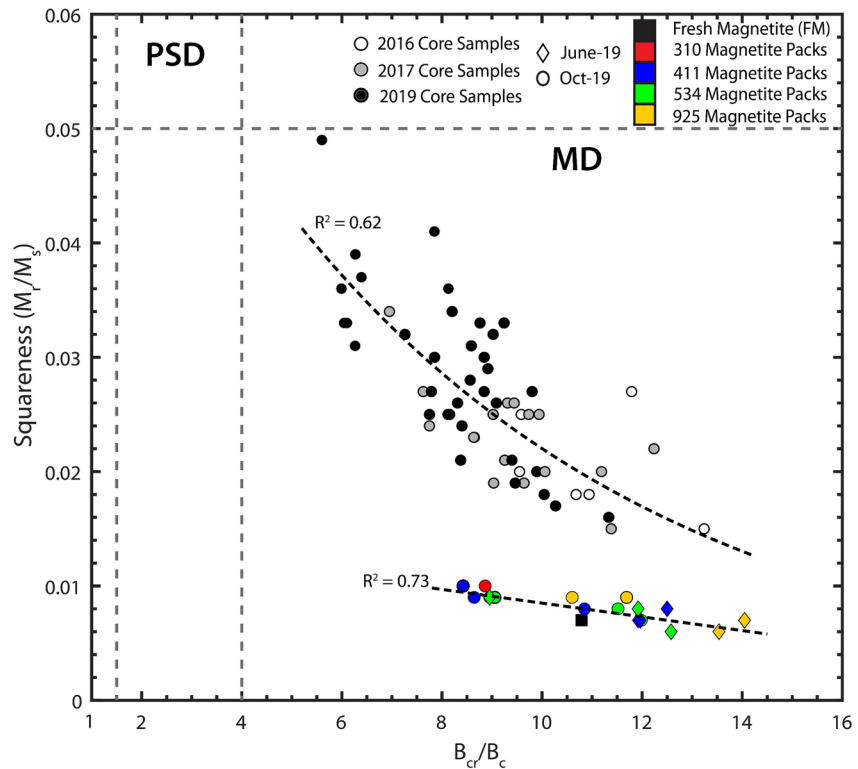
Figure 5. Day plot (ratios of M_r/M_s vs. B_{cr}/B_c) for magnetite packs and core samples (Day et al., 1976). Symbols as in Figures 3 and 4. Dashed lines indicate linear regression fit for the magnetite packs and a second-order polynomial fit for the core samples. MD represents multidomain region and PSD represents pseudo-single domain region.

determined cluster from the demagnetization of anhysteric magnetizations and not from backfield measurements. The second cluster is defined by higher Bh values and a lower DP (~3 mT) and is broadly consistent with the bacterial magnetite components ("biogenic soft (BS)" and "biogenic hard (BH)") described in Egli (2004). All samples from the magnetite packs fall within the region of the detrital component of the natural core samples (Figure 6a). Figure 6b is a plot of the observed contribution (OC) versus distance of the biogenic magnetite from the WTFZ (black circle bounded by red square symbols in Figure 6a). The plot shows that the observed contribution from the biogenic magnetite ranges from about ~50%–80% of the total remanence and appears to decrease with increasing distance from the center of the oil body.

3.1.2. Determination of Magnetic Mineralogy

Low-temperature magnetometry shows a prominent Verwey transition (T_V) at about 120–125 K for both magnetite packs and core samples characteristic of magnetite (Fe_3O_4; Verwey, 1939, Figures 7, 8, S9, and S10 in Supporting Information S1). The magnetite packs within the plume and core samples display similar characteristics, such as the increase in the ratio of FC to ZFC curve at 10K, smearing of the T_V, and an increase in the recovered remanence in heating. These characteristics may be indicative of decreasing grain size and/or partial oxidation of the mineral grains.

For the magnetite packs, the normalized FC-ZFC, warming, and cooling curves for June and October 2019 samples were plotted together with the FM, to more easily identify changes in the samples (Figure 7). In Figure 7, the dotted lines represent FM, dashed lines represent magnetite packs retrieved in June 2019, while solid lines represent magnetite packs retrieved in October 2019. The FC and ZFC curves display similar characteristics for the magnetite packs, with minor deviations from the FM curve (Figures 7a, 7c, and 7g), with the exception of the 534 samples (Figure 7e). The samples have ZFC remanence curves about two times the FC curve, indicative of MD grains, and lose nearly all remanence through the T_V. However, the 534 magnetite pack retrieved in October 2019 retains about 4% of the remanence, which may be negligible, but represents an increase over the other magnetite pack samples (Figure 7e). Another noticeable change is the increase in the ratio of the FC to ZFC curve
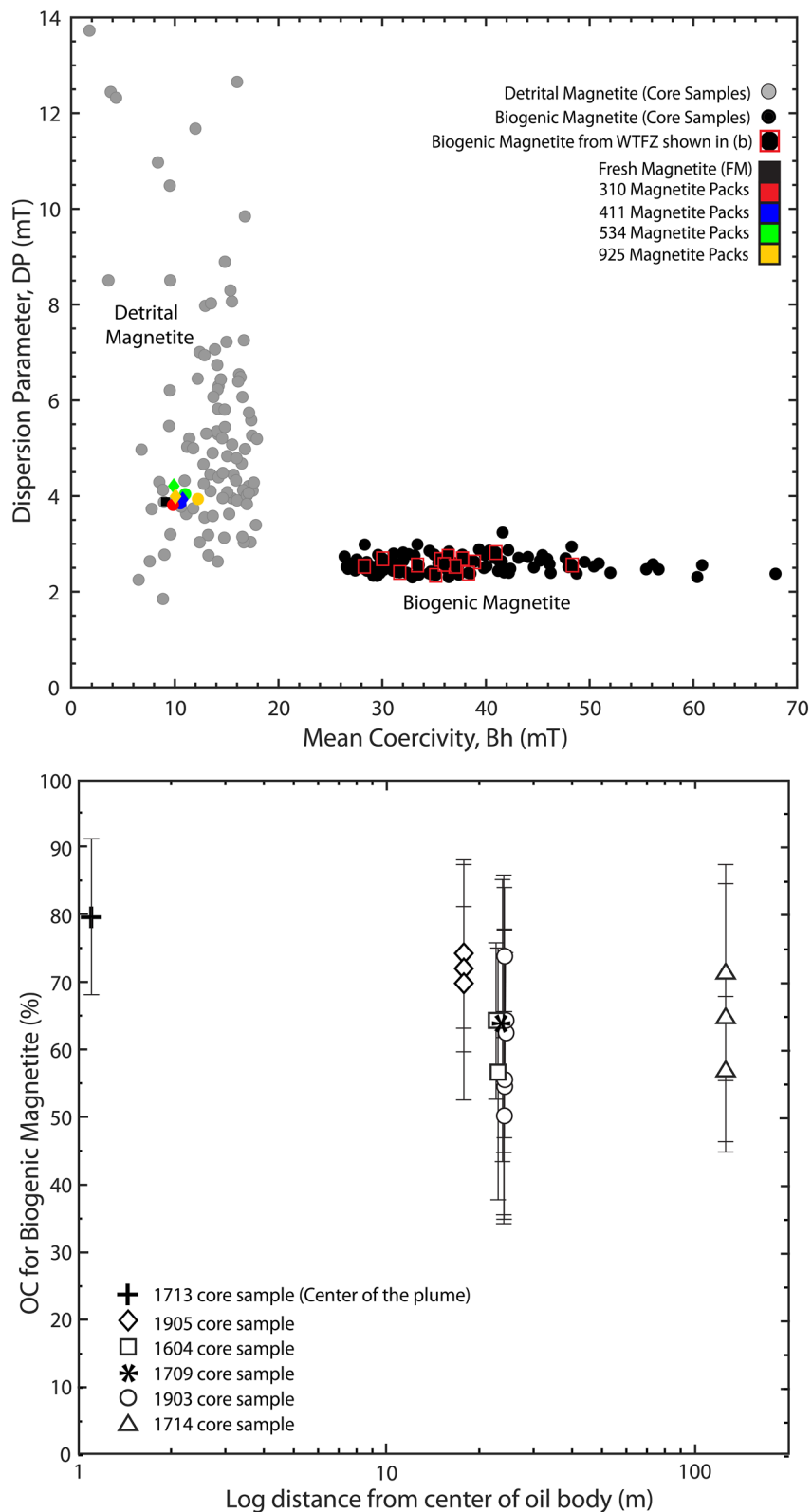
Figure 6. Detrital and authigenic biogenic components of core samples. (a) Plot of dispersion parameter (DP) versus mean coercivity (Bh) for magnetite packs and core samples. Symbols for magnetite packs are as in Figures 3–5. (b) Observed contribution (OC) versus log of distance from the center of the oil body for the biogenic magnetite in the water table fluctuation zone (WTFZ) shown in Figure 6a. The center of the oil body (0 m) is shown in Figure 2. The error bars are the standard deviation for each sample.
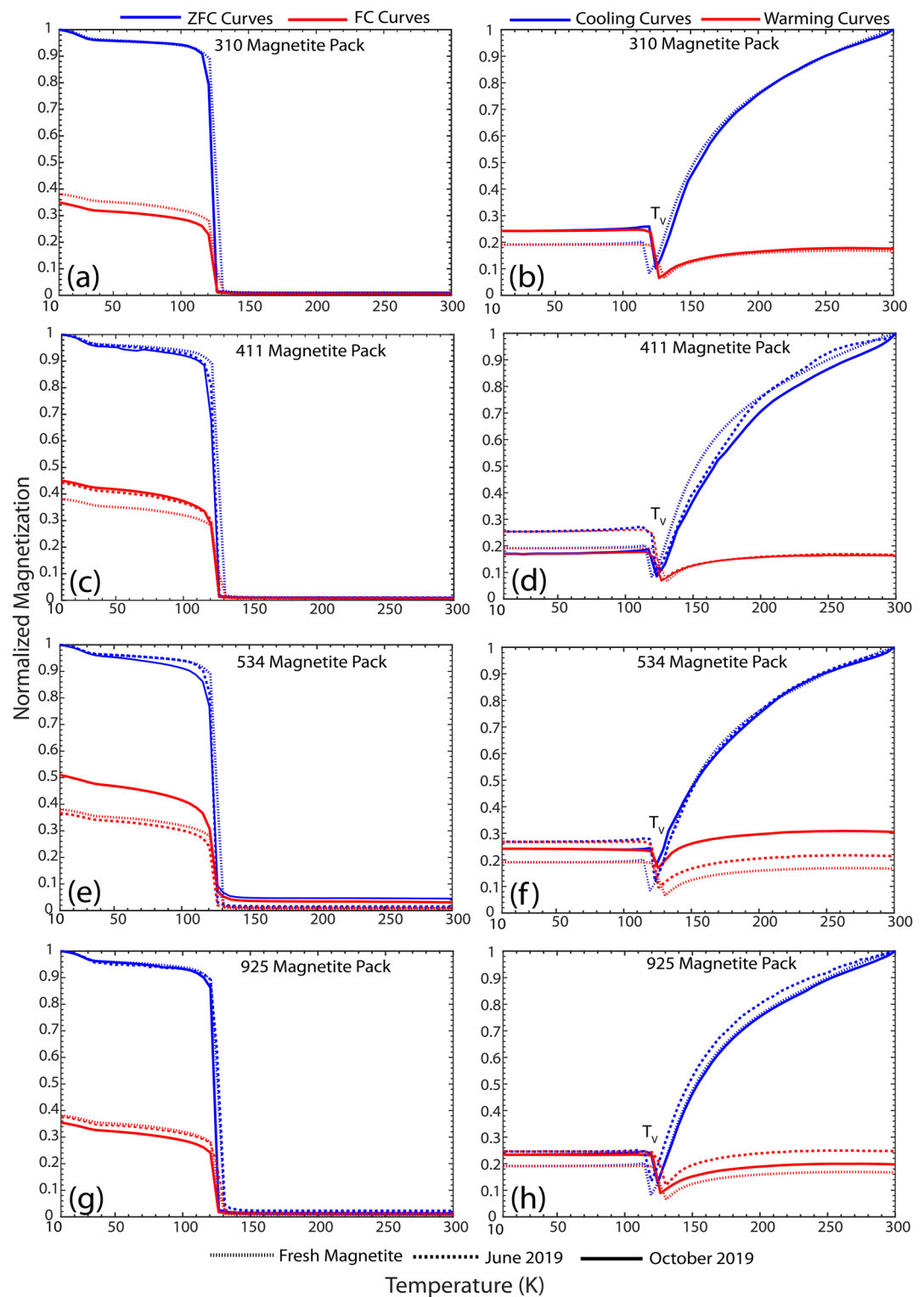
Figure 7. Magnetic characterization of magnetite packs showing ideal magnetite curves. Field-cooled (FC) and zero field-cooled (ZFC) curves for column (a) 310, (c) 411, (e) 534, and (g) 925 magnetite packs. RTSIRM for column (b) 310, (d) 411, (f) 534, and (h) 925 magnetite packs. T_V is the Verwey transition. All magnetite packs shown here are from the central pack above the water table.
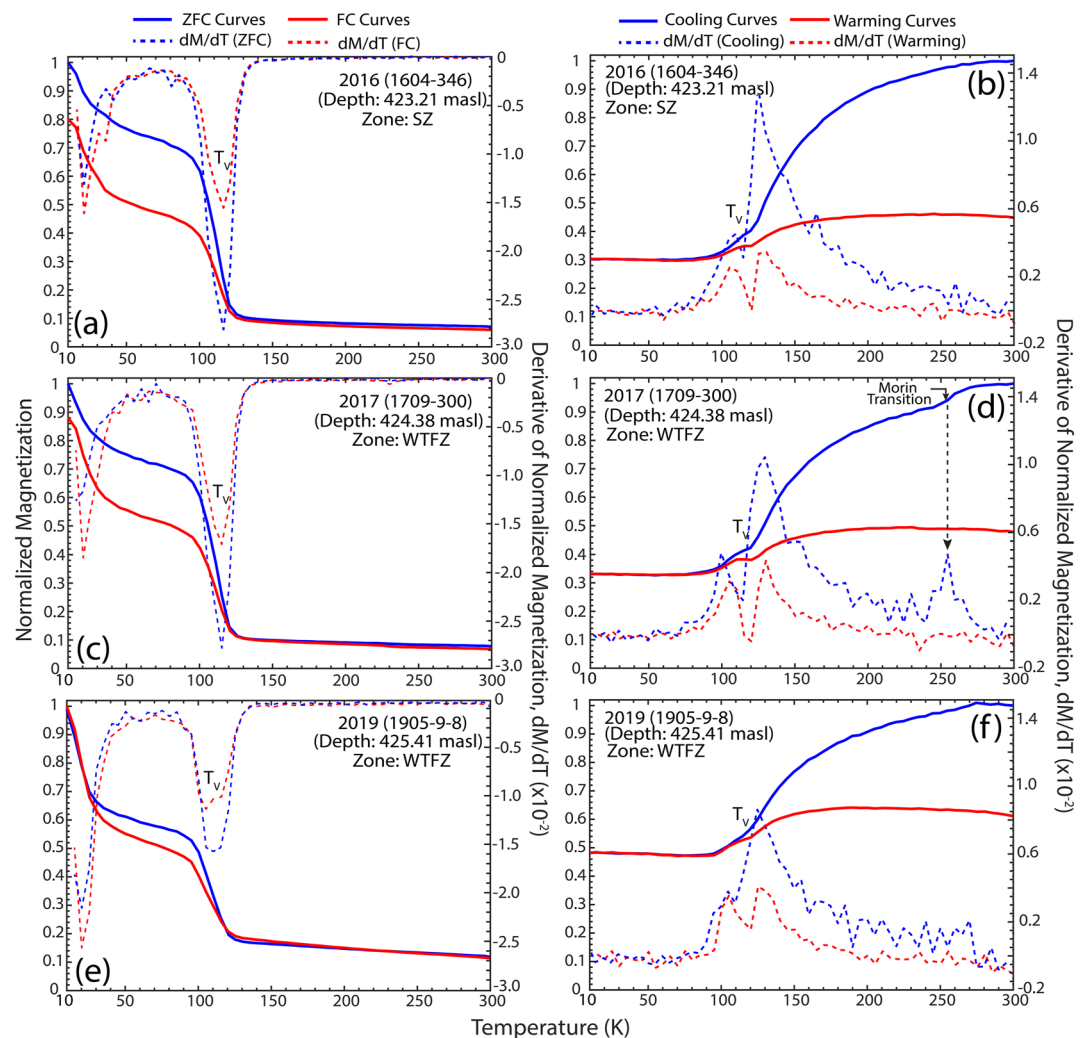
Figure 8. Magnetic characterization of core samples. Field-cooled (FC) and zero field-cooled (ZFC) curves for (a) 1604-346, (c) 1709-300, and (e) 1905-9-8 core samples. Room-temperature pulsed saturation isothermal remanence magnetization for (b) 1604-346, (d) 1709-300, and (f) 1905-9-8 core samples. Depths where the samples were retrieved are shown in the figure and in Table S1 of Supporting Information S1. T_V is the Verwey transition, WTFZ is water table fluctuation zone, and SZ is saturated zone. Solid lines are the measurements and dashed lines are the first derivative of the curves.

at a temperature of 10 K. For the FM curve, this ratio is 0.38; this value decreased slightly or remained constant for the column 310 magnetite pack (with a four-month interment), 534 magnetite pack (retrieved in June 2019), and 925 magnetite packs (retrieved in June and October 2019; Figures 7a, 7e, and 7g, Figure S11a in Supporting Information S1). However, the ratio of the FC to ZFC curve at 10 K increased for magnetite packs within the plume, particularly for samples retrieved in October 2019. The ratio of FC to ZFC curve at 10 K is ∼0.45 for the column 411 magnetite packs (retrieved in June and October 2019) and 0.51 for the 534 magnetite pack (retrieved in October 2019; Figures 7c and 7e, Figure S11a in Supporting Information S1). Since having the ZFC curve higher than the FC curve is indicative of larger-sized multi-domain grains, this increase in the ratio of FC to ZFC curve may be indicative of decreasing grain size and/or partial oxidation.

Cooling curves from RTSIRM experiments show a steady decrease until T_V, where there is a small jump in magnetization (Figures 7b, 7d, 7f, and 7h). Cooling curves for columns 310 and 534 magnetite packs show an almost perfect overlap with the FM cooling curve until T_V (Figures 7b and 7h). In contrast, the cooling curve for the column 411 magnetite pack displays deviations from the FM (Figure 7d). The most striking difference between the FM and magnetite packs for the cooling curve is a reduction in the jump at T_V observed on the column 534 magnetite pack retrieved in October 2019 (Figure 7f). For the warming curves, the magnetization is

constant prior to T_V, and at T_V the magnetization drops. Magnetite pack samples from column 310 display similar curves to the FM and the warming curves almost overlap for these samples; the recovered remanence upon heating is 17% (Figure 7b). This similarity with the FM could be due to the short time the magnetite pack had spent within the well at the site. By contrast, magnetite packs within the plume displayed greater deviation from the FM sample and there is gradual smearing of the T_V most notable in the column 534 magnetite pack (Figure 7f). The 534 magnetite pack also showed the highest recovered remanence during thermal cycling for all magnetite packs measured, about 30% (a single low-temperature magnetometry measurement made on the control ferrihydrite pack is discussed in Text S4 and Figure S3 of Supporting Information S1). These trends are again consistent with decreasing grain size and/or partial oxidation.

The observations highlighted above for the magnetite packs are also noted in the core samples but are more pronounced (Figures 8, S9, and S10 in Supporting Information S1). The core samples show marked differences in the FC-ZFC curves for different samples. The FC-ZFC curve shows a loss in remanence through the T_V, with ~6%–20% retention in remanence. The ratio of FC to ZFC at 10 K ranges from 0.80, indicative of FC below ZFC at 10 K (2016 core sample; Figures 8a and S11b in Supporting Information S1) to 1.48, indicative of FC curve above ZFC curve at 10 K (2019 core sample; Figures S10e and S11b in Supporting Information S1). Generally, the core samples showed no evidence of distinct temporal or depth variations in the ratio of FC to ZFC at 10 K (Figure S11b in Supporting Information S1). The FC-ZFC shows an abrupt remanence decrease from 10 to 20 K, which is probably due to impurities (Chang et al., 2009). To highlight subtle differences between core samples, a plot of δ_{FC} versus δ_{ZFC} is shown in Figure S12 of Supporting Information S1, where δ is defined according to Moskowitz et al. (1993) as a measure of remanence lost by warming through the T_v:

$$\delta = \frac{J_{IRM}(80) - J_{IRM}(150)}{J_{IRM}(80)}, \tag{1}$$

where J_{IRM} refers to the initial SIRM remaining at 80 and 150 K for the FC and ZFC curves. All samples (core samples and magnetite packs) have δ_{FC} less than δ_{ZFC} and thus plot below the δ_{FC} equal to δ_{ZFC} line with a slope of 1.0 (Figure S12 in Supporting Information S1). However, the δ_{FC} and δ_{ZFC} for the magnetite packs have values closer to 1.0 with a range of 0.92–0.99, and the column 534 magnetite pack (October 2019) shows the least value ($\delta_{FC} = 0.92$; $\delta_{ZFC} = 0.95$, Figure S12 in Supporting Information S1). The core samples all have δ less than 0.90, however, the 2019 samples show the least δ for all core samples measured; the only exception to this was a 2017 sample retrieved from the WTFZ (Figure S12 in Supporting Information S1). The reduction in the δ_{FC}/δ_{ZFC} ratio may be indicative of the conversion of the magnetite to maghemite (Moskowitz et al., 1993).

The RTSIRM curves show complete smearing of the T_V and recovered remanence during thermal cycling ranged between 50% and 60%. One of the most striking observations of the RTSIRM curves is the double T_V noted in all the core samples. This double T_V feature is less pronounced on the cooling and warming curves, but is apparent on the first derivative curves (Figures 8, S9, and S10 in Supporting Information S1). The two distinct peaks in T_V were noted at ~100 and ~125 K, which may be indicative of the presence of detrital and biogenic magnetite. Note that we omitted the plot of the first derivative for the magnetite packs, since a plot of the column 534 magnetite pack retrieved in October 2019, which showed the greatest deviation from the FM, did not exhibit major changes when compared to the FM (Figure S8 in Supporting Information S1). Additionally, sample 1709-300 (2017 core sample) shows a Morin transition at 250 K associated with the presence of hematite in the sample (Figure 8d).

The thermomagnetic behavior of the samples is characterized by a magnetite mineral, with a Curie temperature of about 580–600°C for the 2016 and 2017 core samples (Figure S13 in Supporting Information S1). There is also an observed increase in the heating runs at about 500°C, which may be attributed to the neoformation of magnetite due to thermal alteration (Figure S13 in Supporting Information S1, Yang et al., 2011). However, this observation is significantly diminished or absent in the 2017 samples retrieved from the dissolved phase of the plume (Figures S13e and S13f in Supporting Information S1).

3.2. Determination of Spatial and Depth Variability in Magnetization

Box plots from the ANOVA for the M_s of the core samples of different depths and the magnetite packs are shown in Figure S14 of Supporting Information S1. Tables 1 and 2 contain the output of the formal ANOVA test. For the magnetite packs, the ANOVA test indicates that the differences between the M_s of the different magnetite packs

Table 1
*Output of the Analysis of Variance for Magnetite Packs With a Statistically Significant p-Value*

Descriptive statistics					
R-square	0.966				
Mean of response	7.092				
Observations	210				

Analysis of variance (ANOVA)					
	Degrees of freedom	Sum of squares	Mean square	F ratio	Prop > F
Depth (between groups)	3	8830.979	2943.66	1958.577	<0.0001
Error (within groups)	206	309.610	1.500		
C. total	209	9140.589			

Means of oneway ANOVA					
Magnetite packs	*N*	Mean	Std error	Lower 95%	Upper 95%
Fresh magnetite (FM)	30	22.681	0.224	22.24	23.122
411	60	2.741	0.158	2.429	3.053
534	60	4.735	0.158	4.423	5.047
925	60	6.004	0.158	5.692	6.316

are statistically significant ($P < 0.0001$). Figure S14b in Supporting Information S1 shows the comparison of the means using a Tukey-Kramer HSD to compare the means and explore the statistical significance of the difference between the means. The result shows that the means of all samples are statistically different from one another, indicated by the lack of overlapping circles (Figure S14b in Supporting Information S1). For the core samples, the ANOVA test indicates that differences between the M_s of core samples retrieved from the UVZ, LVZ, WTFZ, and SZ are not statistically different ($P = 0.64$). This was expected as the box plot shows overlapping boxes and/or whiskers (Figure S14c in Supporting Information S1).

Table 2
Output of the Analysis of Variance for the Core Samples With a Statistically Insignificant p-Value

Descriptive statistics					
R-square	0.055				
Mean of response	0.109				
Observations	33				

Analysis of variance (ANOVA)					
	Degrees of freedom	Sum of squares	Mean square	F ratio	Prop > F
Depth (between groups)	3	0.008	0.0026	0.5661	0.6417
Error (within groups)	29	0.134	0.0046		
C. total	32	0.141			

Means of oneway ANOVA					
Depths	*N*	Mean	Std error	Lower 95%	Upper 95%
UVZ	6	0.105	0.028	0.049	0.162
LVZ	12	0.128	0.020	0.088	0.168
WTFZ	9	0.090	0.023	0.044	0.137
SZ	6	0.102	0.028	0.046	0.159

Note. UVZ is the upper vadose zone, LVZ is lower vadose zone, WTFZ is the water table fluctuation zone, and SZ is the saturated zone.
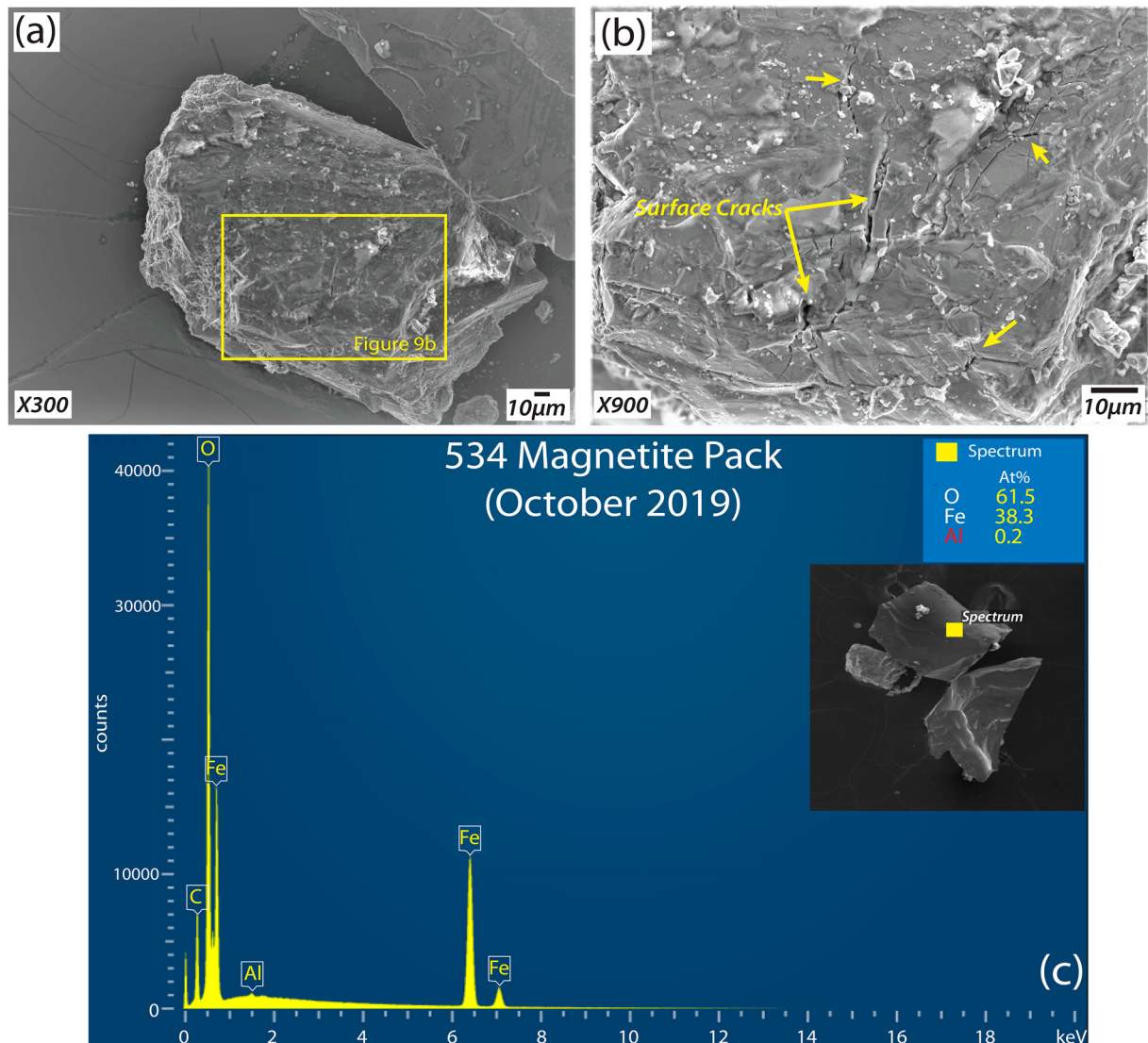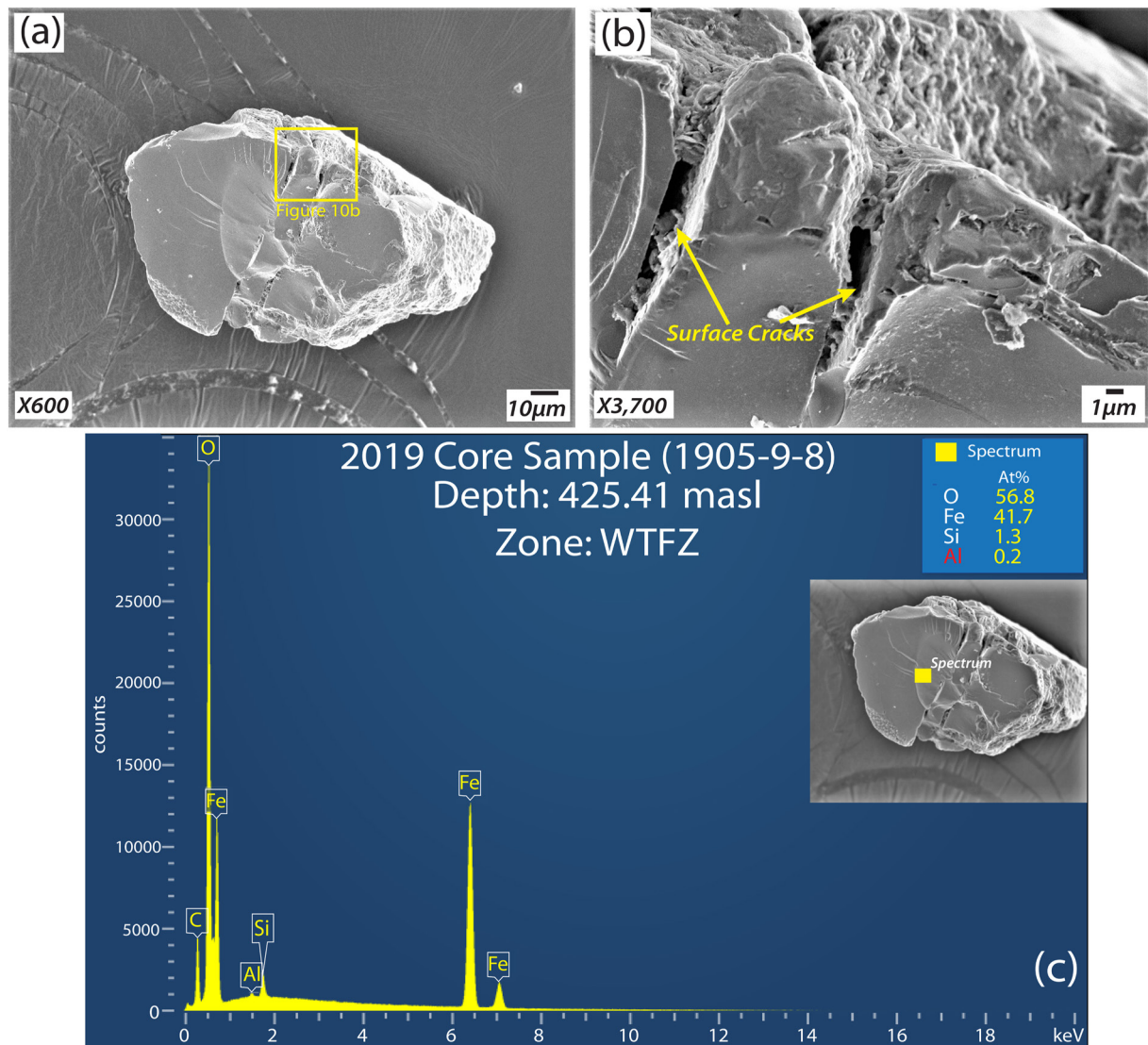
Figure 9. Scanning electron microscope (SEM) micrographs showing cracking on the surface due to maghemitization and energy-dispersive X-ray spectroscopy (EDS) analysis of magnetic mineral separated from the October 2019 column 534 magnetite pack. (a) SEM micrographs at x300 magnification. Yellow rectangle is shown in Figure 9b. (b) Surface of mineral sample at x900 magnification. Yellow arrows point to cracking on the surface of the grain. (c) EDS analysis of the surface layer of inset image.

3.3. SEM Imaging and EDS Analyses

The selection of samples for electron microscopy was guided by the results of the low-temperature magnetometry. We performed SEM imaging of the magnetite packs on the FM sample and the column 534 magnetite pack since it showed the greatest deviation from the FM and represents a suitable representative for samples within the plume. SEM imaging of the magnetite packs revealed two distinct types of mineral grains: (a) angular-shaped magnetic minerals (Figure S15a in Supporting Information S1), and (b) aggregates of cubic grains ~180 μm in diameter (Figure S15b in Supporting Information S1). These two populations were present in all the magnetite packs analyzed. The SEM micrographs of the isolated October 2019 column 534 magnetite pack grains showed considerable variations from the FM. While the SEM micrograph of the FM showed no observable surface alteration (Figures S15c and S15d in Supporting Information S1), the SEM micrographs for the October 2019 column 534 magnetite pack showed pronounced roughness and shrinkage cracking on the surface of the grains (Figures 9a and 9b). The measurable cracks on the surface of the column 534 magnetite packs vary between 1

Figure 10. Scanning electron microscope (SEM) micrographs showing cracking on the surface due to maghemitization and energy-dispersive X-ray spectroscopy (EDS) analysis of magnetic mineral separated from the 2019 core sample 1905-9-8 retrieved from an elevation of 425.41 masl. (a) SEM micrographs at x600 magnification. Yellow rectangle is shown in Figure 10b. (b) surface of mineral sample at x3700 magnification. (c) EDS analysis of the surface layer of inset image. WTFZ is water table fluctuation zone.

and 2.35 μm. EDS analyses indicate that the major elements are O and Fe, with an O to Fe ratio of 62%–38% (Figure 9c), with minor concentrations of aluminum (Al) and carbon (C; Figure 9c).

SEM micrographs were also collected from the 2019 sediment core samples. Isolated magnetic grains also show shrinkage cracking on the surface of the grains, with deep grooves that appear to extend into the interior of the mineral, with minor infillings of clay minerals (Figures 10a and 10b). EDS analyses show the magnetic mineral is an iron oxide, with minor elements such as Al and Si (Figure 10c).

4. Discussion

4.1. Magnetic Mineral Phases

Past research has reported several Fe-bearing minerals to be associated with hydrocarbon-contaminated sediments, including magnetite (Ameen et al., 2014; Rijal et al., 2012), maghemite, hematite (Emmerton et al., 2013), ferrihydrite, siderite, and ferran calcite (Baedecker et al., 1993; Tuccillo et al., 1999).

At the Bemidji site, low-temperature magnetometry measurements indicate that the dominant magnetic mineral is a magnetite/magnetite-like mineral identifiable by a prominent T_V in all core samples measured (Figures 8, S8, and S9 in Supporting Information S1). The derivative curves of low-temperature magnetometry show two distinct magnetite components apparent as a double T_V in the RTSIRM measurements of the core samples (Figures 8, S8, and S9 in Supporting Information S1). We observe two distinct peaks of T_V at ∼100 and ∼125 K, associated with the presence of biogenic and inorganic (or detrital) magnetite, respectively (Chang et al., 2016). This identification is consistent with previous studies which found authigenic magnetite within the WTFZ to be directly responsible for magnetic susceptibility enhancement at the site (Atekwana et al., 2014; Lund et al., 2017). Magnetic measurements of the core samples were not limited to samples from the WTFZ but included samples below and above this zone, and within and outside the plume. The core samples from different zones and locations across the plume showed minor differences in the FC-ZFC and RTSIRM curves (Figures S11 and S12 in Supporting Information S1). The ANOVA test performed on the 2019 core samples retrieved from different depths within the plume indicate that the M_s values for the samples are not statistically different, indicative of similarities between magnetite retrieved from different depths (Table 2).

Maghemite, $\gamma - Fe_2^{3+}O_3$, is also present at the Bemidji site. Maghemite is a partially oxidized or cation-deficient form of magnetite (Dunlop & Özdemir, 1997). Maghemite may be created via a variety of different pathways, including the dehydroxylation of lepidocrocite, but the most common formation method of maghemite is the topotactic oxidation of magnetite (Cornell & Schwertmann, 2003). Magnetic evidence for the formation of maghemite includes (a) decreasing M_s (Figures 3a and 3c, Dunlop & Özdemir, 1997), (b) increasing coercivities (Figures 3b, 3d, and 4, Özdemir et al., 1993), (c) increasing remanence retention during RTSIRM experiments (Figures 7 and 8), (d) the suppression of T_v in the RTSIRM curves (Figures 7f and 8), and (e) the near unity value of the ratio of δ_{FC} to δ_{ZFC} (Figure S12 in Supporting Information S1). This is caused by the deviations from stoichiometric magnetite, which have a pronounced effect on the T_V (Özdemir et al., 1993) or disruption of chain structure (Moskowitz et al., 1993). These observations were conspicuous in the core samples and less pronounced in the magnetite packs. SEM micrographs and EDS analyses also provide evidence for maghemite at the site via the appearance of shrinkage cracks on crystal surfaces in both the magnetite pack and core samples (Figures 9 and 10). Furthermore, quantification of the elemental composition for the samples provides conclusive affirmation with the ratio of Fe to O of ∼40%–60%, characteristic of maghemite.

The other magnetic mineral identified at the site is hematite, identified by the Morin transition at ∼250 K (Figures 8d and Morin, 1950). The presence of hematite is noted in only the 2017 sample retrieved within the WTFZ. Since this was recorded in just a single sample from the nine core samples measured and magnetite packs, it is unclear how and when the hematite formed.

4.2. Magnetic Mineral Transformation and Loss of Magnetization

The magnetite packs and core samples show a decrease in magnetization with time (Figures 3 and 4), which is consistent with the observations of Lund et al. (2017) (Figure S4 in Supporting Information S1). The column 310 magnetite pack, outside the plume with the least interment (four-months) showed the least decrease in magnetization, considering FM as the starting value. The magnetite packs within the plume (columns 411 and 534 magnetite packs) showed the greatest loss in magnetization. Magnetite packs for the columns 411 and 534 retrieved after seven months showed a 55%–68% loss in magnetization, while samples retrieved after 11 months showed a ∼90% loss in magnetization. Under varying environmental conditions, there are several distinct factors or a combination of factors that may lead or contribute to the loss of magnetization, such as iron reduction, mineral dissolution, and iron oxidation. Each of these factors possesses a distinctive magnetic and mineralogical signature and the presence or absence of certain iron minerals serves as litmus tests for a number of reaction(s) that may be occurring at this site.

The reduction of magnetite to siderite ($FeCO_3$) has been the dominant hypothesis for the loss of magnetization at this site (Atekwana et al., 2014; Lund et al., 2017). Siderite is paramagnetic at ordinary temperatures and therefore expected to have low M_s (Dunlop & Özdemir, 1997) and relatively low magnetic susceptibility between $13–110 \times 10^{-4}$ SI (Dearing, 1994). This hypothesis is appealing because it agrees with existing microbial and geochemical observations at the site. Some of this evidence includes the existence of specific bacteria, such as *Geobacter*, known to reduce magnetite (Beaver et al., 2016; Byrne et al., 2015, 2016). The geochemistry of the

site also favors this hypothesis, the anoxic (dissolved oxygen = 0–0.1 mg/L; USGS, 2021), neutral pH (6.2–6.8; USGS, 2021) conditions, and depletion of solid-phase Fe(III); Lund et al., 2017) at the site are thermodynamically suitable for siderite and/or vivianite (Porsch et al., 2010). However, the magnetic measurements suggest no evidence of either siderite or vivianite in the samples that were examined in this current study. The presence of siderite is detectable in low-temperature magnetometry marked by the presence of Néel transition (T_N) at a temperature of ~38 K (Housen et al., 1996; Jacobs, 1963). However, there is no evidence for T_N in the measured magnetite packs and core samples examined in this study. Vivianite ($Fe_3[PO_4]_2 \cdot 8H_2O$) has a Néel temperature <15 K (Frederichs et al., 2003), which was not observed in any of the low-temperature measurements of this study. Further, geochemistry data at the Bemidji site show no evidence of phosphate in the environment. Iron reduction is known to sometimes produce secondary iron sulfides (pyrrhotite, greigite, and pyrite), depending on available electron donors and the prevailing conditions (Hansel et al., 2003). The monoclinic 4C pyrrhotite polytype possesses a magnetic transition temperature of ~32 K (Koulialias et al., 2019; Volk et al., 2018) which was absent in low-temperature magnetometry measurements. Further, pseudohexagonal pyrrhotite displays the "lambda transition" at temperatures between 200 and 250°C which was absent in high-temperature susceptibility measurements on core samples, suggesting no evidence of magnetic iron sulfides (Figure S13 in Supporting Information S1). Although greigite does not show any known low-temperature transition (Chang et al., 2009), its absence and that of other sulphate minerals could be inferred by the low sulphate concentrations measured in this aquifer, typically between 0.5 and 5 mg/L. Amos et al. (2012) found these concentrations were too low to explain anaerobic oxidation of simple hydrocarbons in this system. Additionally, the ferrihydrite packs showed no considerable enhanced magnetization (Figure S2 in Supporting Information S1). This is important since we expect the Fe (III) available in ferrihydrite to be bioavailable for reduction. However, the only reaction observed was the transformation of ferrihydrite to goethite, also noted in the control ferrihydrite (Figure S3 in Supporting Information S1). Hence, although reduction may be one of the processes occurring at the site, it is not likely related to the loss of magnetization at the locations examined in this study.

Dissolution of magnetite and other magnetic minerals at the site is another process that may contribute to the loss of magnetization at the site. Mineral dissolution has been identified as one of the ongoing processes at the Bemidji site (Delin et al., 1998) and the strongly anoxic conditions known to occur within the center of the plume (Figure 2) are consistent with the occurrence of magnetite dissolution. The reductive dissolution of magnetite by *Geobacter sulfurreducens* (Byrne et al., 2016; Kostka & Nealson, 1995) or the transformation of magnetite to hematite via dissolution and reprecipitation (Lagoeiro, 1998) is also possible and would account for the precipitous decrease in M_s observed in the magnetite packs within the plume as well as account for the hematite observed in the 2017 core sample. It is possible that dissolution of nanometer-sized microbially mediated magnetite around 2011 resulted in the loss of magnetic susceptibility subsequently recorded in 2014 and 2015. Evidence of dissolution at the site can be inferred from decreasing grain size noted in several magnetic measurements. This decrease in grain size is observed from the increase in B_c associated with decreasing M_s noted in both the core samples and magnetite packs (Figure 3). The plot of the squareness (M_r/M_s) and B_c for the magnetite packs shows a progression toward higher squareness (M_r/M_s) and B_c with time, indicative of decreasing grain size (Figure 4b). Additionally, the increasing ratio of FC to ZFC with time for magnetite packs within the plume is evidence of decreasing grain size or partial oxidation (Figure S11a in Supporting Information S1). This decrease in grain size and the substantial drop in M_s values observed within the plume are possible evidence of dissolution at the site and may play an important role at some places within the Bemidji site, as discussed below.

Maghemitization is undoubtedly contributing to the loss of magnetization at the site with evidence provided from both magnetic measurements and electron microscopy. Maghemitization is frequently thought of as a low-temperature oxidation or weathering process that occurs mostly on mineral surfaces. Maghemite is a relatively common oxide mineral alteration product (Dunlop & Özdemir, 1997; Özdemir et al., 1993). The mechanism for maghemitization is the diffusion of Fe^{2+} from the interior of a magnetite grain to a free surface converting the magnetite to maghemite (Dunlop & Özdemir, 1997):

$$4Fe_3O_4 + O_2 \rightarrow 6Fe_2O_3 \tag{2}$$

Magnetic and EDS analysis of the magnetite packets and core samples confirms the presence of maghemite at the site, with all the core samples measured showing the magnetic hallmarks of maghemitization and maghemite discussed in Section 4.1 (Figures 8, S9, and S10 in Supporting Information S1, Özdemir & Dunlop, 2010).

Additionally, the appearance of shrinkage cracks on the surface similar to the observations of Dunlop and Özdemir (1997) is evidence supporting maghemitization of magnetite crystals at the site (Figures 9 and 10). Although maghemitization is an active process occurring everywhere at the Bemidji site, it cannot account for the ~90% drop in M_s recorded in magnetite packs within the free phase of the plume. The M_s of maghemite is generally ~20% less than that of magnetite (Dunlop & Özdemir, 1997), and so even if all of the magnetite was converted to maghemite, it would be impossible to account for a 90% decrease. Thus, within the plume, we must invoke mineral dissolution to account for the drop in magnetization. Mineral dissolution may not be occurring outside of the plume, as maghemitization could account for the much lower ~10% loss in M_s in the magnetite packs.

However, the evidence for co-occurrence of both maghemitization and magnetite dissolution at Bemidji is confounding. Maghemitization is typically thought of as a process occurring in oxygen-rich environments (Cornell & Schwertmann, 2003), whereas magnetite dissolution occurs primarily in anoxic environments. Geochemical measurements reveal that the center of the Bemidji plume is highly anoxic. One possible explanation that would allow maghemitization within an anoxic plume is that magnetite is losing electrons (oxidizing) as part of microbial cycling occurring at the site. In short, we hypothesize microbially induced anaerobic oxidation of magnetite.

4.3. Microbial Influence on Magnetic Mineral Transformation

Unmixed coercivity spectra show two distinct magnetic components in the core samples, which we interpret as low coercivity detrital and high-coercivity biogenic magnetite (Figure 6a). The detrital component that we interpret here is consistent with populations of large grains within the glacial outwash sediment at the Bemidji site. The high coercivity component is consistent with microbially mediated magnetite produced in situ within the sediment after deposition. The percentage of remanence held by the high coercivity biogenic component within the smear zone is highest at the center of the oil body ($80 \pm 11\%$, 1713) and shows minor decrease with increasing distance from the center of the oil (Figure 6b). Similar observation of detrital and biogenic magnetite was also obtained from the low-temperature magnetometry discussed in Section 4.1. Despite the evidence for the occurrence of biogenic magnetite, whose production is possibly mediated by microbial communities associated with the hydrocarbon contamination, an outstanding question that persists is, can microorganisms be simultaneously responsible for both the production of magnetite and its oxidation (maghemitization) at the site?

Magnetic and microbial evidence from the site supports the plausibility of microbially induced oxidation of magnetite. Magnetic evidence supporting microbial oxidation at the site can be inferred from the ANOVA test performed on the magnetite packs and core samples. For the magnetite packs, the ANOVA test shows that a spatial relationship exists for the samples in relation to the center of the plume. The enhanced decrease in M_s for magnetite packs in the zone containing the free phase (the pit) compared to column 925 magnetite pack in the dissolved phase of the plume (with higher oxygen concentration) may be indicative of enhanced microbial oxidation at the center of the plume (Bekins et al., 2005) combined with dissolution. Similarly, although the core samples showed no depth relationship in the ANOVA test, the M_s of samples within the WTFZ had the lowest mean value (Table 2 and Figure S6 in Supporting Information S1). Atekwana et al. (2014) showed that the WTFZ is a zone of microbial enrichment and MS values were highest within the WTFZ in 2011 and ascribed to the microbial precipitation of magnetite. The statistical non-significance of the ANOVA performed on the core samples and failure to infer any depth variability in the core samples are significant here since they suggest reaction(s) intrinsic to the WTFZ (perhaps dissolution and oxidation) influencing the loss in magnetization at the site. The lower M_s value for samples within the WTFZ compared to other zones in 2019 (Figure S6 in Supporting Information S1) despite the enhanced MS in 2011 (Figure S4 in Supporting Information S1) provides supporting evidence of a bioreactive WTFZ that decreased the magnetization beyond the already low magnetization observed in the other zones (UVZ, LVZ, SZ). This hypothesis of enhanced oxidation by microbial activity in the oil zone is supported by the MS-temperature curves (Figure S13 in Supporting Information S1). The samples within the area with free-phase hydrocarbons (1604 and 1713) show a relatively higher Curie temperature and larger observed increase in susceptibility in the heating curves at 500°C (Figures S13a–S13d in Supporting Information S1) compared to samples within the dissolved phase of the plume (Figures S13e and S13f in Supporting Information S1). This increase in the susceptibility at 500°C is related to the inversion of maghemite or titanomaghemite to a stable phase Fe mineral (perhaps hematite) at temperatures above 250°C and is dependent on the degree of oxidation of the maghemite (Özdemir, 1987; Özdemir & Banerjee, 1984). Thus, the differences observed in samples within

the free-phase area and the dissolved phase of the plume and the generally higher Curie temperatures may be indicative of a higher degree of oxidation promoted by microbial action in samples within the anoxic free phase of the plume.

Microbial studies at the site confirm the existence of an iron-oxidizer *Rhodopseudomonas* capable of oxidizing magnetite (Beaver et al., 2021). *Rhodopseudomonas* has been shown in laboratory experiments to oxidize magnetite, even in environments devoid of molecular oxygen, leading to a loss in MS (Byrne et al., 2015, 2016). However, the microbiology data do not show any known iron oxidizer within the WTFZ. Instead, the zone is dominated by methanogens and their syntropic partners and the iron-oxidizing bacteria *Rhodopseudomonas* was found above the WTFZ (Beaver et al., 2021). Its occurrence at the site points to a possible pathway for microbial oxidation. Another hypothesis is that iron oxidation may be a product of the switch in metabolism noted in methanogens. Recent studies indicate that methanogens are capable of switching their metabolism between methanogenesis and iron reduction (Beaver et al., 2021; Sivan et al., 2016). This hypothesis of a switch in reaction may be a possible pathway to anaerobic oxidation at the site. Beaver et al. (2021) postulate an exchange of electrons between methanogens and iron oxidizers on opposite ends of the magnetite within the WTFZ, with the magnetite acting as a conductor. If this is the case, the high magnetization observed in 2011 may be associated with the dominance of the methanogens primarily carrying out iron reduction. A switch in the metabolism from iron reduction to methanogenesis after 2011 may allow for iron oxidation to dominate this electron transfer process promoting maghemitization and causing a decrease in magnetization.

Iron oxides such as magnetite and maghemite have been shown to enhance direct interspecies electron transfer (DIET) particularly in syntrophic-methanogenic associations (Xu et al., 2019). The co-occurrence of the methanogenic zone and iron oxide enrichment within the WTFZ suggests some influence of anaerobic digestion that produces methane using the magnetite at this site. Current studies on DIET have focused on the impact of different iron oxides on the syntrophic methanogenic communities and not on how the DIET affects the magnetic properties of the iron oxides (Li et al., 2015; Xu et al., 2019). Thus, we speculate a net oxidation effect on the iron oxides, which acts as an electrical bridge mediating electron transfer from donors to acceptors (Li et al., 2015).

One potential limitation of this study is the nature of the magnetite used in the magnetite packs. The measured M_s of the fresh 5% magnetite-95% quartz sediment pack (22.68 A.m.^{2} kg^{-1}) is significantly higher than the expected theoretical value of ~4.6 A.m.^{2} kg^{-1} for a sediment containing 5% magnetite (Dunlop & Özdemir, 1997). The higher than expected M_s value suggests that either magnetite was concentrated beyond 5% in the fresh magnetite sample, or that the magnetite samples used for this study contained traces of minerals with higher M_s values (such as might occur if the magnetite was produced from the oxidation of iron). This ambiguity limits our ability to use decreasing M_s values to estimate the relative contributions of dissolution and oxidation. However, the stability of the control sample, the lateral variability observed in the magnetite packs within the plume, and the lack of depth variability in the 2019 core samples is unmistakable evidence that dissolution and oxidation are both occurring within the WTFZ of the plume center and are jointly responsible for the rapid decline in M_s. In this study, we focused on the maghemitization part of the reaction over the dissolution because dissolution in a hydrocarbon-contaminated aquifer is an expected reaction and does not present an anomaly. Furthermore, dissolution reaction is a fixed process at the site and was occurring during the observed waxing (reduction reaction) of magnetization. Thus, its presence alone cannot account for the waning of magnetization and the occurrence of maghemite at the site. One way dissolution and maghemitization may both promote the loss of magnetization at the site is enhanced dissolution along the weaker crystal zones caused by the cracking on the surface of the grains due to maghemitization, this dissolution and downgradient transportation may limit the relative abundance of maghemite.

Previous arguments against microbial oxidation as the cause for the loss of magnetization at the site cited the anoxic conditions within the plume (Lund et al., 2017). Microbially mediated anaerobic oxidation of magnetite at the site would overcome such arguments. Bryce et al. (2018) reported microorganisms and mechanisms for the anaerobic oxidation of magnetite related to nitrate reduction to form N_2. Nitrate concentrations at the site are low typically <1 mg/L (Cozzarelli et al., 1994), and N_2 gas data from the site are inconclusive but show elevated quantities of N_2 at discrete locations near the plume (USGS, 2020). The magnetic and scanning electron microscopy results presented in this study are most harmoniously interpreted within the context of microbially induced anaerobic oxidation at the Bemidji site. However, further microbial and geochemistry studies are needed to link specific iron oxidizers and identify potential oxidants associated with the loss in magnetization and MS at the site.

5. Conclusions

The magnetic data from the Bemidji site provide evidence for iron mineral transformations that account for the loss of magnetization previously recorded and observed in magnetite packs and core samples retrieved from the site. Within the center of the plume, we observe dissolution and maghemitization of magnetite. Outside of the plume, we observe only maghemitization. However, the origin of the maghemitization may be different within and outside of the plume. The maghemitization occurring outside of the plume results in only minor losses of magnetization and is likely associated with abiotic oxidation. The maghemitization inside the plume observed via magnetic measurements and scanning electron microscopy is occurring within a zone known to be strongly anoxic and, we hypothesize, is the result of microbially mediated anaerobic oxidation. Yet, the dramatic loss of magnetization in magnetite packs interred within the plume cannot be explained solely by maghemitization and suggest that mineral dissolution enhanced by crack formation during maghemitization is also occurring. While iron-oxidizing microorganisms have been identified at the Bemidji site, they have not yet been identified within the WTFZ and remain a focus for future microbiological studies at the site.

Disclaimer

Any use of trade, firm, or product names is for descriptive purposes only and does not imply endorsement by the U.S. Government.

Data Availability Statement

The magnetic data used in this study can be obtained from https://doi.org/10.17632/mg5wj5d486.2.

References

Abbas, M., Jardani, A., Machour, N., & Dupont, J. P. (2018). Geophysical and geochemical characterisation of a site impacted by hydrocarbon contamination undergoing biodegradation. *Near Surface Geophysics*, *16*(2), 176–192. https://doi.org/10.3997/1873-0604.2017061

Ameen, N. N., Klueglein, N., Appel, E., Petrovský, E., Kappler, A., & Leven, C. (2014). Effect of hydrocarbon-contaminated fluctuating groundwater on magnetic properties of shallow sediments. *Studia Geophysica et Geodaetica*, *58*(3), 442–460. https://doi.org/10.1007/s11200-014-0407-3

Amos, R. T., Bekins, B. A., Cozzarelli, I. M., Voytek, M. A., Kirshtein, J. D., Jones, E. J. P., & Blowes, D. W. (2012). Evidence for iron-mediated anaerobic methane oxidation in a crude oil-contaminated aquifer. *Geobiology*, *10*(6), 506–517. https://doi.org/10.1111/j.1472-4669.2012.00341.x

Anderson, R. T., & Lovley, D. R. (2000). Anaerobic bioremediation of benzene under sulfate-reducing conditions in a petroleum-contaminated aquifer. *Environmental Science and Technology*, *34*(11), 2261–2266. https://doi.org/10.1021/es991211a

Aristovskaya, T. V. (1974). Role of microorganisms in iron mobilization and stabilization in soils. *Geoderma*, *12*, 145–150. https://doi.org/10.1016/0016-7061(74)90046-9

Atekwana, E. A., & Atekwana, E. A. (2010). Geophysical signatures of microbial activity at hydrocarbon contaminated sites: A review. *Surveys in Geophysics*, *31*(2), 247–283. https://doi.org/10.1007/s10712-009-9089-8

Atekwana, E. A., Mewafy, F. M., Aal, G. A., Werkema, D. D., Jr., Revil, A., & Slater, L. D. (2014). High-resolution magnetic susceptibility measurements for investigating magnetic mineral formation during microbial mediated iron reduction. *Journal of Geophysical Research: Biogeosciences*, *119*, 80–94. https://doi.org/10.1002/2013JG002414

Baedecker, M. J., Cozzarelli, I. M., Eganhouse, R. P., Siegel, D. I., & Bennett, P. C. (1993). Crude oil in a shallow sand and gravel aquifer—III. Biogeochemical reactions and mass balance modeling in anoxic groundwater. *Applied Geochemistry*, *8*(6), 569–586. https://doi.org/10.1016/0883-2927(93)90014-8

Baedecker, M. J., Cozzarelli, I. M., Evans, J. R., & Hearn, P. P. (1992). Authigenic mineral formation in aquifers rich in organic material. In Y. K. Kharaka, A. S. M. Rotterdam, & A. A. Balkema (Eds.), *Proceedings of the 7th international symposium on water-rock interaction*. (pp. 257–261).

Baedecker, M. J., Eganhouse, R. P., Qi, H., Cozzarelli, I. M., Trost, J. J., & Bekins, B. A. (2018). Weathering of oil in a surficial aquifer. *Groundwater*, *56*(5), 797–809. https://doi.org/10.1111/gwat.12619

Beaver, C. L., Atekwana, E. A., Bekins, B. A., Ntarlagiannis, D., Slater, L. D., & Rossbach, S. (2021). Methanogens and their syntrophic partners dominate zones of enhanced magnetic susceptibility at a petroleum contaminated site. *Frontiers of Earth Science*, *9*, 1–18. https://doi.org/10.3389/feart.2021.598172

Beaver, C. L., Williams, A. E., Atekwana, E. A., Mewafy, F. M., Abdel Aal, G., Slater, L. D., & Rossbach, S. (2016). Microbial communities associated with zones of elevated magnetic susceptibility in hydrocarbon-contaminated sediments. *Geomicrobiology Journal*, *33*(5), 441–452. https://doi.org/10.1080/01490451.2015.1049676

Bekins, B. A., Cozzarelli, I. M., Erickson, M. L., Steenson, R. A., & Thorn, K. A. (2016). Crude oil metabolites in groundwater at two spill sites. *Groundwater*, *54*(5), 681–691. https://doi.org/10.1111/gwat.12419

Bekins, B. A., Hostettler, F. D., Herkelrath, W. N., Delin, G. N., Warren, E., & Essaid, H. I. (2005). Progression of methanogenic degradation of crude oil in the subsurface. *Environmental Geosciences*, *12*(2), 139–152. https://doi.org/10.1306/eg.11160404036

Bennett, P. C., Siegel, D. E., Baedecker, M. J., & Hult, M. F. (1993). Crude oil in a shallow sand and gravel aquifer-I. Hydrogeology and inorganic geochemistry. *Applied Geochemistry*, *8*(6), 529–549. https://doi.org/10.1016/0883-2927(93)90012-6

Bryce, C., Blackwell, N., Schmidt, C., Otte, J., Huang, Y. M., Kleindienst, S., et al. (2018). Microbial anaerobic Fe(II) oxidation—Ecology, mechanisms and environmental implications. *Environmental Microbiology*, *20*(10), 3462–3483. https://doi.org/10.1111/1462-2920.14328

Byrne, J. M., Klueglein, N., Pearce, C., Rosso, K. M., Appel, E., & Kappler, A. (2015). Redox cycling of Fe(II) and Fe(III) in magnetite by Fe-metabolizing bacteria. *Science (New York, N.Y.)*, *347*(6229), 1473–1476. https://doi.org/10.1126/science.aaa4834

Byrne, J. M., Van Der Laan, G., Figueroa, A. I., Qafoku, O., Wang, C., Pearce, C. I., et al. (2016). Size dependent microbial oxidation and reduction of magnetite nano-and micro-particles. *Scientific Reports*, *6*, 1–13. https://doi.org/10.1038/srep30969

Chang, L., Heslop, D., Roberts, A. P., Rey, D., & Mohamed, K. J. (2016). Discrimination of biogenic and detrital magnetite through a double Verwey transition temperature. *Journal of Geophysical Research: Solid Earth*, *121*, 3–14. https://doi.org/10.1002/2015JB012485

Chang, L., Roberts, A. P., Rowan, C. J., Tang, Y., Pruner, P., Chen, Q., & Horng, C. S. (2009). Low-temperature magnetic properties of greigite (Fe$_3$S$_4$). *Geochemistry, Geophysics, Geosystems*, *10*, Q01Y04. https://doi.org/10.1029/2008GC002276

Cornell, R. M., & Schwertmann, U. (2003). *The iron oxides: Structure, properties, reactions, occurrences, and uses* (2nd ed.). Wiley-VCH. https://doi.org/10.1002/3527602097

Cozzarelli, I. M., Baedecker, M. J., Eganhouse, R. P., & Goerlitz, D. F. (1994). The geochemical evolution of low-molecular-weight organic acids derived from the degradation of petroleum contaminants in groundwater. *Geochimica et Cosmochimica Acta*, *58*(2), 863–877. https://doi.org/10.1016/0016-7037(94)90511-8

Cozzarelli, I. M., Bekins, B. A., Eganhouse, R. P., Warren, E., & Essaid, H. I. (2010). In situ measurements of volatile aromatic hydrocarbon biodegradation rates in groundwater. *Journal of Contaminant Hydrology*, *111*(1–4), 48–64. https://doi.org/10.1016/j.jconhyd.2009.12.001

Cozzarelli, I. M., Schreiber, M. E., Erickson, M. L., & Ziegler, B. A. (2016). Arsenic cycling in hydrocarbon plumes: Secondary effects of natural attenuation. *Groundwater*, *54*(1), 35–45. https://doi.org/10.1111/gwat.12316

Day, R., Fuller, M. D., & Schmidt, V. A. (1976). Magnetic hysteresis of synthetic titanomagnetites. *Journal of Geophysical Research*, *81*(5), 873–880. https://doi.org/10.1029/JB081i005p00873

Dearing, J. A. (1994). *Environmental magnetic susceptibility: Using the Bartington MS2 system*. Chi Publishing.

Delin, G. N., Essaid, H. I., Cozzarelli, I. M., Lahvis, M. H., & Bekins, B. A. (1998). Ground water contamination by crude oil near Bemidji, Minnesota. U.S. Geological Survey Fact Sheet FS-084-98, 4. https://doi.org/10.3133/fs08498

Delin, G. N., & Herkelrath, W. N. (2017). Effects of crude oil on water and tracer movement in the unsaturated and saturated zones. *Journal of Contaminant Hydrology*, *200*, 49–59. https://doi.org/10.1016/j.jconhyd.2017.03.007

Dunlop, D. J., & Özdemir, O. (1997). *Rock magnetism: Fundamentals and frontiers* (No. 3). Cambridge University Press.

Egli, R. (2004). Characterization of individual rock magnetic components by analysis of remanence curves. 2. Fundamental properties of coercivity distributions. *Physics and Chemistry of the Earth*, *29*(13–14), 851–867. https://doi.org/10.1016/j.pce.2004.04.001

Emmerton, S., Muxworthy, A. R., Sephton, M. A., Aldana, M., Costanzo-Alvarez, V., Bayona, G., & Williams, W. (2013). Correlating biodegradation to magnetization in oil bearing sedimentary rocks. *Geochimica et Cosmochimica Acta*, *112*, 146–165. https://doi.org/10.1016/j.gca.2013.03.008

Essaid, H. I., Bekins, B. A., Herkelrath, W. N., & Delin, G. N. (2011). Crude oil at the Bemidji site: 25 years of monitoring, modeling, and understanding. *Ground Water*, *49*(5), 706–726. https://doi.org/10.1111/j.1745-6584.2009.00654.x

Fahrenfeld, N., Cozzarelli, I. M., Bailey, Z., & Pruden, A. (2014). Insights into biodegradation through depth-resolved microbial community functional and structural profiling of a crude-oil contaminant plume. *Microbial Ecology*, *68*(3), 453–462. https://doi.org/10.1007/s00248-014-0421-6

Frederichs, T., von Dobeneck, T., Bleil, U., & Dekkers, M. J. (2003). Towards the identification of siderite, rhodochrosite, and vivianite in sediments by their low-temperature magnetic properties. *Physics and Chemistry of the Earth*, *28*(16–19), 669–679. https://doi.org/10.1016/S1474-7065(03)00121-9

Hansel, C. M., Benner, S. G., & Fendorf, S. (2005). Competing Fe (II) -Induced mineralization pathways of ferrihydrite. *Environmental Science & Technology*, *39*(18), 7147–7153. https://doi.org/10.1021/es050666z

Hansel, C. M., Benner, S. G., Neiss, J., Dohnalkova, A., Kukkadapu, R. K., & Fendorf, S. (2003). Secondary mineralization pathways induced by dissimilatory iron reduction of ferrihydrite under advective flow. *Geochimica et Cosmochimica Acta*, *67*(16), 2977–2992. https://doi.org/10.1016/S0016-7037(03)00276-X

Heslop, D., & Dillon, M. (2007). Unmixing magnetic remanence curves without a priori knowledge. *Geophysical Journal International*, *170*(2), 556–566. https://doi.org/10.1111/j.1365-246X.2007.03432.x

Housen, B. A., Banerjee, S. K., & Moskowitz, B. M. (1996). Low-temperature magnetic properties of siderite and magnetite in marine sediments. *Geophysical Research Letters*, *23*(20), 2843–2846. https://doi.org/10.1029/96GL01197

Ionescu, D., Heim, C., Polerecky, L., Thiel, V., & De Beer, D. (2015). Biotic and abiotic oxidation and reduction of iron at circumneutral pH are inseparable processes under natural conditions. *Geomicrobiology Journal*, *32*(3–4), 221–230. https://doi.org/10.1080/01490451.2014.887393

Jackson, M., & Solheid, P. (2010). On the quantitative analysis and evaluation of magnetic hysteresis data. *Geochemistry, Geophysics, Geosystems*, *11*(4). https://doi.org/10.1029/2009GC002932

Jacobs, I. S. (1963). Metamagnetism of siderite (FeCO$_3$). *Journal of Applied Physics*, *34*, 1106–1107. https://doi.org/10.1063/1.1729389

Kappler, A., & Bryce, C. (2017). Cryptic biogeochemical cycles: Unravelling hidden redox reactions. *Environmental Microbiology*, *19*(3), 842–846. https://doi.org/10.1111/1462-2920.13687

Kappler, A., Bryce, C., Mansor, M., Lueder, U., Byrne, J. M., & Swanner, E. D. (2021). An evolving view on biogeochemical cycling of iron. *Nature Reviews Microbiology*, *19*(6), 360–374. https://doi.org/10.1038/s41579-020-00502-7

Kostka, J. E., & Nealson, K. H. (1995). Dissolution and reduction of magnetite by bacteria. *Environmental Science and Technology*, *29*(10), 2535–2540. https://doi.org/10.1021/es00010a012

Koulialias, D., Lesniak, B., Schwotzer, M., Weidler, P. G., Löffler, J. F., & Gehring, A. U. (2019). The Besnus transition in single-domain 4C pyrrhotite. *Geochemistry, Geophysics, Geosystems*, *20*(11), 5216–5224. https://doi.org/10.1029/2019GC008627

Lagoeiro, L. E. (1998). Transformation of magnetite to hematite and its influence on the dissolution of iron oxide minerals. *Journal of Metamorphic Geology*, *16*(3), 415–423. https://doi.org/10.1111/j.1525-1314.1998.00144.x

Li, H., Chang, J., Liu, P., Fu, L., Ding, D., & Lu, Y. (2015). Direct interspecies electron transfer accelerates syntrophic oxidation of butyrate in paddy soil enrichments. *Environmental Microbiology*, *17*(5), 1533–1547. https://doi.org/10.1111/1462-2920.12576

Li, L., Steefel, C. I., Williams, K. H., Wilkins, M. J., & Hubbard, S. S. (2009). Mineral transformation and biomass accumulation associated with uranium bioremediation at Rifle, Colorado. *Environmental Science & Technology*, *43*(14), 5429. https://doi.org/10.1021/es900016v

Liu, L., Jia, Z., Tan, W., Suib, S. L., Ge, L., Qiu, G., & Hu, R. (2018). Abiotic photomineralization and transformation of iron oxide nanominerals in aqueous systems. *Environmental Science: Nano*, *5*(5), 1169–1178. https://doi.org/10.1039/c7en01242j

Liu, Q., Roberts, A. P., Larrasoaa, J. C., Banerjee, S. K., Guyodo, Y., Tauxe, L., & Oldfield, F. (2012). Environmental magnetism: Principles and applications. *Reviews of Geophysics*, *50*(4), 1–50. https://doi.org/10.1029/2012RG000393

Lovley, D. R. (1990). Magnetite formation during microbial dissimilatory iron reduction. In R. B. Frankel, & R. P. Blakemore (Eds.), *Iron biominerals* (pp. 151–166). https://doi.org/10.1007/978-1-4615-3810-3_11

Lund, A. L., Slater, L. D., Atekwana, E. A., Ntarlagiannis, D., Cozzarelli, I., & Bekins, B. A. (2017). Evidence of coupled carbon and iron cycling at a hydrocarbon-contaminated site from time lapse magnetic susceptibility. *Environmental Science and Technology*, *51*(19), 11244–11249. https://doi.org/10.1021/acs.est.7b02155

Markovski, C., Byrne, J. M., Lalla, E., Lozano-Gorrín, A. D., Klingelhöfer, G., Rull, F., et al. (2017). Abiotic versus biotic iron mineral transformation studied by a miniaturized backscattering Mössbauer spectrometer (MIMOS II), X-ray diffraction and Raman spectroscopy. *Icarus*, *296*, 49–58. https://doi.org/10.1016/j.icarus.2017.05.017

Maxbauer, D. P., Feinberg, J. M., & Fox, D. L. (2016a). Magnetic mineral assemblages in soils and paleosols as the basis for paleoprecipitation proxies: A review of magnetic methods and challenges. *Earth-Science Reviews*, *155*, 28–48. https://doi.org/10.1016/j.earscirev.2016.01.014

Maxbauer, D. P., Feinberg, J. M., & Fox, D. L. (2016b). Max UnMix: A web application for unmixing magnetic coercivity distributions. *Computers & Geosciences*, *95*, 140–145. https://doi.org/10.1016/j.cageo.2016.07.009

McAllister, S. M., Barnett, J. M., Heiss, J. W., Findlay, A. J., MacDonald, D. J., Dow, C. L., et al. (2015). Dynamic hydrologic and biogeochemical processes drive microbially enhanced iron and sulfur cycling within the intertidal mixing zone of a beach aquifer. *Limnology & Oceanography*, *60*(1), 329–345. https://doi.org/10.1002/lno.10029

Mewafy, F. M., Atekwana, E. A., Werkema, D. D., Slater, L. D., Ntarlagiannis, D., Revil, A., et al. (2011). Magnetic susceptibility as a proxy for investigating microbially mediated iron reduction. *Geophysical Research Letters*, *38*(21), 1–5. https://doi.org/10.1029/2011GL049271

Morin, F. J. (1950). Magnetic susceptibility of αFe_2O_3 and αFe_2O_3 with added titanium. *Physical Review*, *78*(6), 819–820. https://doi.org/10.1103/PhysRev.78.819.2

Moskowitz, B., Frankel, R. B., & Bazylinski, D. A. (1993). Rock magnetic criteria for the detection of biogenic magnetite. *Earth and Planetary Science Letters*, *120*, 283–300. https://doi.org/10.1016/0012-821x(93)90245-5

Murphy, F., & Herkelrath, W. N. (1996). A sample-freezing drive shoe for a wire line piston core sampler. *Groundwater Monitoring & Remediation*, *16*(3), 86–90. https://doi.org/10.1111/j.1745-6592.1996.tb00143.x

Özdemir, Ö. (1987). Inversion of titanomaghemites. *Physics of the Earth and Planetary Interiors*, *46*(1–3), 184–196. https://doi.org/10.1016/0031-9201(87)90181-6

Özdemir, Ö., & Banerjee, S. K. (1984). High temperature stability of maghemite (γ-Fe_2O_3). *Geophysical Research Letters*, *11*(3), 161–164.

Özdemir, Ö., & Dunlop, D. J. (2010). Hallmarks of maghemitization in low-temperature remanence cycling of partially oxidized magnetite nanoparticles. *Journal of Geophysical Research*, *115*(B2), 1–10. https://doi.org/10.1029/2009jb006756

Özdemir, Ö., Dunlop, D. J., & Moskowitz, B. M. (1993). The effect of oxidation on the verwey transition in magnetite. *Geophysical Research Letters*, *20*(16), 1671–1674.

Porsch, K., Dippon, U., Rijal, M. L., Appel, E., & Kappler, A. (2010). In-situ magnetic susceptibility measurements as a tool to follow geomicrobiological transformation of Fe minerals. *Environmental Science and Technology*, *44*(10), 3846–3852. https://doi.org/10.1021/es903954u

Rawson, J., Prommer, H., Siade, A., Carr, J., Berg, M., Davis, J. A., & Fendorf, S. (2016). Numerical modeling of arsenic mobility during reductive iron-mineral transformations. *Environmental Science and Technology*, *50*(5), 2459–2467. https://doi.org/10.1021/acs.est.5b05956

Rijal, M. L., Appel, E., Petrovský, E., & Blaha, U. (2010). Change of magnetic properties due to fluctuations of hydrocarbon contaminated groundwater in unconsolidated sediments. *Environmental Pollution*, *158*(5), 1756–1762. https://doi.org/10.1016/j.envpol.2009.11.012

Rijal, M. L., Porsch, K., Appel, E., & Kappler, A. (2012). Magnetic signature of hydrocarbon-contaminated soils and sediments at the former oil field Hänigsen, Germany. *Studia Geophysica et Geodaetica*, *56*(3), 889–908. https://doi.org/10.1007/s11200-010-0040-8

Sivan, O., Shusta, S. S., & Valentine, D. L. (2016). Methanogens rapidly transition from methane production to iron reduction. *Geobiology*, *14*(2), 190–203. https://doi.org/10.1111/gbi.12172

Telford, W. M., Geldart, L. P., & Sheriff, R. E. (1990). *Applied geophysics* (2nd ed.). Cambridge University Press.

Truskewycz, A., Gundry, T. D., Khudur, L. S., Kolobaric, A., Taha, M., Aburto-Medina, A., et al. (2019). Petroleum hydrocarbon contamination in terrestrial ecosystems—Fate and microbial responses. *Molecules*, *24*(18), 1–20. https://doi.org/10.3390/molecules24183400

Tuccillo, M. E., Cozzarelli, I. M., & Herman, J. S. (1999). Iron reduction in the sediments of a hydrocarbon-contaminated aquifer. *Applied Geochemistry*, *14*(5), 655–667. https://doi.org/10.1016/S0883-2927(98)00089-4

U.S. Geological Survey. (2020). U.S. Geological Survey Bemidji Project Web Page. Retrieved from https://mn.water.usgs.gov/projects/bemidji/spatial/index.html

U.S. Geological Survey. (2021). U.S. Geological Survey Bemidji Project Web Page. Retrieved from https://mn.water.usgs.gov/projects/bemidji/spatial/index.html

Verwey, E. (1939). Electronic conduction of magnetite (Fe_3O_4) and its transition point at low temperatures. *Nature*, *144*, 327–328. https://doi.org/10.1038/144327b0

Volk, M. W. R., McCalla, E., Voigt, B., Manno, M., Leighton, C., & Feinberg, J. M. (2018). Changes in physical properties of 4C pyrrhotite (Fe_7S_8) across the 32 K Besnus transition. *American Mineralogist*, *103*(10), 1674–1689. https://doi.org/10.2138/am-2018-6514

Wang, D., & Van der Voo, R. (2004). The hysteresis properties of multidomain magnetite and titanomagnetite/titanomaghemite in mid-ocean ridge basalts. *Earth and Planetary Science Letters*, *220*(1–2), 175–184. https://doi.org/10.1016/S0012-821X(04)00052-4

Xu, H., Chang, J., Wang, H., Liu, Y., Zhang, X., Liang, P., & Huang, X. (2019). Enhancing direct interspecies electron transfer in syntrophic-methanogenic associations with (semi)conductive iron oxides: Effects and mechanisms. The *Science of the Total Environment*, *695*, 133876. https://doi.org/10.1016/j.scitotenv.2019.133876

Yang, T., Zeng, Q., Liu, Z., & Liu, Q. (2011). Magnetic properties of the road dusts from two parks in Wuhan city, China: Implications for mapping urban environment. *Environmental Monitoring and Assessment*, *177*, 637–648. https://doi.org/10.1007/s10661-010-1662-6

References From the Supporting Information

Bertotti, G. (1998). *Hysteresis in magnetism: For physicists, materials scientists, and engineers* (Ser. Electromagnetism). Academic Press.

Özdemir, Ö., & Dunlop, D. J. (1996). Thermoremanence and Néel temperature of goethite. *Geophysical Research Letters*, *23*(9), 921–924. https://doi.org/10.1029/96GL00904

Tauxe, L., Bertram, H. N., & Seberino, C. (2002). Physical interpretation of hysteresis loops: Micromagnetic modeling of fine particle magnetite. *Geochemistry, Geophysics, Geosystems*, *3*(10), 1055. https://doi.org/10.1029/2001GC000241